JM PAPERS

Generalised Jeffery's equations for rapidly spinning particles. Part 2. Helicoidal objects with chirality

M.P. Dalwadi[1,2,†], C. Moreau[3], E.A. Gaffney[4], B.J. Walker[1,5] and K. Ishimoto[3]

[1]Department of Mathematics, University College London, London WC1H 0AY, UK

[2]Mathematical Institute, University of Oxford, Oxford OX2 6GG, UK

[3]Research Institute for Mathematical Sciences, Kyoto University, Kyoto 606-8502, Japan

[4]Wolfson Centre for Mathematical Biology, Mathematical Institute, University of Oxford, Oxford OX2 6GG, UK

[5]Department of Mathematical Sciences, University of Bath, Bath BA2 7AY, UK

In this two-part study, we investigate the motion of rigid, active objects in shear Stokes flow, focusing on bodies that induce rapid rotation as part of their activity. In Part 2, we derive and analyse governing equations for rapidly spinning complex-shaped particles – general helicoidal objects with chirality. Using the multiscale framework that we develop in Part 1 (Dalwadi *et al.*, *J. Fluid Mech.*, vol. 979, 2024, A1), we systematically derive emergent equations of motion for the angular and translational dynamics of these chiral spinning objects. We show that the emergent dynamics due to rapid rotation can be described by effective generalised Jeffery's equations, which differ from the classic versions via the inclusion of additional terms that account for chirality and other asymmetries. Furthermore, we use our analytic results to characterise and quantify the explicit effect of rotation on the effective hydrodynamic shape of the chiral objects, expanding significantly the scope of Jeffery's seminal study.

1. Introduction

The complex dynamics of objects in fluid flow is known to depend strongly on an object's shape, with the early study of Jeffery (1922) capturing explicitly the behaviour of passive

† Email address for correspondence: m.dalwadi@ucl.ac.uk

spheroidal particles in shear Stokes flow. Later extensions by Bretherton (1962) and Brenner (1964*a*) widen the range of passive objects to which Jeffery's approach applies, with geometry playing a fundamental role in determining the dynamics.

In this two-part study, we consider the emergent dynamics of rigid active objects. Inspired by the locomotion of flagellated bacterial swimmers (Marcos *et al.* 2012), we consider swimmers whose activity consists of rapid rotation while propelling themselves through the surrounding fluid. In Part 1 (Dalwadi *et al.* 2023), we developed a multiscale framework to analyse rapidly rotating particles in Stokes flow, and applied it to investigate spheroidal objects in shear flow, which follow Jeffery's equations. Here, in Part 2, we broaden our analysis to general helicoidal objects (described in detail below), including chiral particles, whose passive dynamics are governed by generalised versions of Jeffery's equations (Ishimoto 2020*a,b*). The dynamics of chiral bodies is generally more intricate than for achiral bodies since chiral objects induce additional hydrodynamic interactions. The importance of chiral effects has been identified and utilised in theoretical and experimental studies across many different areas, including the drift-induced separation of chiral objects (Marcos *et al.* 2009; Eichhorn 2010; Aristov, Eichhorn & Bechinger 2013; Ro, Yi & Kim 2016), chirality-affected rheotaxis in bacterial and artificial swimmers (Marcos *et al.* 2012; Mathijssen *et al.* 2019; Jing *et al.* 2020; Khatri & Burada 2022; Zöttl *et al.* 2022; Zheng *et al.* 2023), the migration of chiral DNA-like objects (Chen & Zhang 2011), and the preferential rotation of chiral dipoles (Kramel *et al.* 2016).

Certain geometric symmetries generate specific simplifications to the hydrodynamic resistance tensor associated with the object in Stokes flow. However, while the hydrodynamic resistance tensor depends strongly on an object's geometry, it does not define the shape uniquely. That is, there exist objects with the same simplified hydrodynamic resistance tensor but without the associated geometric symmetries. Sharing the same form of the hydrodynamic resistance tensor defines a hydrodynamic symmetry. Importantly, this means that there is a difference between the hydrodynamic symmetry of an object – the properties of its dynamics in flow – and its geometric features.

In Part 2 of this two-part study, we consider swimmers that possess helicoidal hydrodynamic symmetry about a swimmer-fixed axis, and we refer to objects that satisfy this type of symmetry as helicoidal objects. This symmetry, introduced by Brenner (1964*a,b*) and recounted recently by Ishimoto (2020*a*), generalises the geometric notion of rotational symmetry in the context of fluid mechanics. Specifically, helicoidal symmetry means that the hydrodynamic resistance tensor associated with the object is invariant under rotations by $\pm\beta$ about a swimmer-fixed axis for some fixed $\beta \notin \{0, \pi, 2\pi/3\}$ (with the excluded cases noted to be degenerate by Brenner 1964*a*).

The distinction between hydrodynamic and geometric symmetry is important because it is not straightforward to characterise geometrically the properties of an object with hydrodynamic symmetry. For example, objects that have *n*-fold rotational symmetry for some $n \geqslant 4$ are hydrodynamically helicoidal (Brenner 1964*b*; Ishimoto 2020*b*), but objects with geometric helical symmetry (e.g. a simple helix of finite length) are not helicoidal in general. Of particular note, while axisymmetric objects follow Jeffery's equations as stated by Bretherton (1962), not all objects governed by Jeffery's equations are axisymmetric. In light of this, we characterise the particles described by the analysis of Part 1 of this two-part study (i.e. those that follow Jeffery's equations) as 'Jeffery bodies'. We emphasise that this definition includes simple spheroids.

The general active helicoidal objects that we consider in this part are generalised versions of these Jeffery bodies. As identified in Ishimoto (2020*b*), the dynamics of a passive helicoidal particle in shear flow is governed by generalised Jeffery orbits

comprising six characteristic parameters, in contrast to only one for Jeffery bodies (the Bretherton parameter B). When we introduce the governing dynamical system for active particles later, we discuss the role of these six parameters, along with subcases of interest and correspondences with geometric symmetries of the object. A detailed discussion of chirality, general helicoidal objects, and their associated contributions to the governing equations of motion for passive objects can be found in Ishimoto (2020*a*).

In our study, we specifically allow the axis of the self-propelled spinning to deviate from the axis of symmetry, as is the case for a wiggling bacterium (Hyon *et al.* 2012; Thawani & Tirumkudulu 2018) and a wobbling magnetised helix (Man & Lauga 2013). In these contexts, the time scale of activity-driven spinning is typically much faster than that of reorientation by an imposed flow field. Motivated by these separated time scales, we analyse the dynamics using the asymptotic method of multiple scales (Hinch 1991; Bender & Orszag 1999), as in Part 1 and several recent works (Gaffney *et al.* 2022; Ma, Pujara & Thiffeault 2022; Walker *et al.* 2022*a*). In particular, we derive effective governing equations for the emergent dynamics, accounting systematically for the complex nonlinear interaction between rapid rotation and the slower effects of the flow.

Hence, in this second part of our two-part study, we consider the dynamics of a three-dimensional, self-propelled chiral object with helicoidal symmetry, undergoing rapid spinning due to its own activity, and interacting with an externally imposed three-dimensional shear flow. In § 2, we present the general governing equations for the system, including additional terms not present in Part 1 that account for chirality and other asymmetries of the object. In § 3, we set up the machinery for our multiple scales analysis, then in §§ 4 and 5, we perform the analysis for both rotation and translation, respectively, systematically deriving effective governing equations that capture explicitly the effects of rapid spinning on the overall dynamics. As one may expect, the effective dynamics that we derive for general helicoidal particles in Part 2 are significantly richer than those that we derive for simple spheroidal particles in Part 1. Hence we summarise the key physical results and implications of the emergent dynamics that we derive through our analysis in a non-technical manner in § 6. Finally, we conclude with a discussion of our study in § 7.

2. Governing equations

Our physical set-up in Part 2 is similar to that in Part 1, but now with a more complex swimmer geometry. That is, we now consider a general helicoidal swimmer, as discussed in § 1, in the presence of a far-field shear flow. This will result in additional hydrodynamic effects due to object chirality and other asymmetries. We scale time with inverse shear rate, and space with a characteristic swimmer length, working in dimensionless quantities henceforth. Specifically, we consider the motion of a rigid, self-propelled helicoidal object in a shear flow, which has swimming velocity V and angular velocity $\boldsymbol{\Omega}$ in a quiescent fluid. As before, these propulsion and rotation vectors are fixed in direction and magnitude in a swimmer-fixed basis, but the orientation of this swimmer basis will vary rapidly in the laboratory frame through its dependence on $\boldsymbol{\Omega}$.

We define the swimmer-fixed axis of helicoidal symmetry by $\hat{\boldsymbol{e}}_1$. Therefore, we may take $\hat{\boldsymbol{e}}_2$ such that the self-generated angular velocity $\boldsymbol{\Omega}$ is in a plane spanned by $\hat{\boldsymbol{e}}_1$ and $\hat{\boldsymbol{e}}_2$, where $\boldsymbol{\Omega}$ makes an angle α with $\hat{\boldsymbol{e}}_1$. Therefore, we may write $\boldsymbol{\Omega} = \Omega_\parallel \hat{\boldsymbol{e}}_1 + \Omega_\perp \hat{\boldsymbol{e}}_2$, with $\Omega_\parallel$ and $\Omega_\perp$ being the constant components of angular velocity that are parallel and perpendicular, respectively, to the axis of helicoidal symmetry. This generates the relationship $\tan \alpha = \Omega_\perp / \Omega_\parallel$. We then define $\hat{\boldsymbol{e}}_3 = \hat{\boldsymbol{e}}_1 \times \hat{\boldsymbol{e}}_2$. In this swimmer-fixed basis, we write the self-generated propulsion $V = V_1 \hat{\boldsymbol{e}}_1 + V_2 \hat{\boldsymbol{e}}_2 + V_3 \hat{\boldsymbol{e}}_3$. The position of
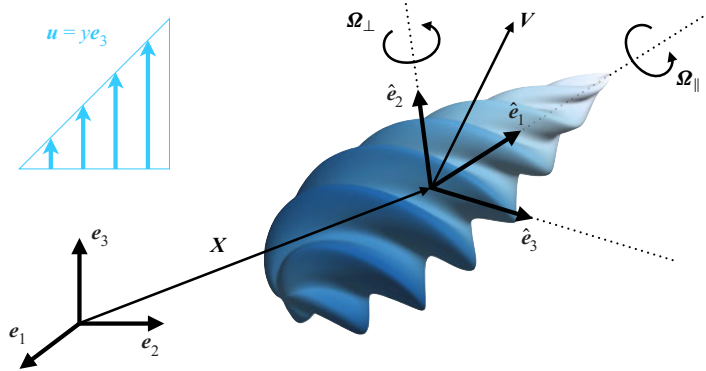
Figure 1. A schematic of the notation and the physical set-up that we consider in Part 2. We investigate the dynamics of a chiral, helicoidal swimmer with axis of symmetry $\hat{e}_1$. The swimmer has self-generated translational and rotational velocities $V = V_1\hat{e}_1 + V_2\hat{e}_2 + V_3\hat{e}_3$ and $\boldsymbol{\Omega} = \Omega_\parallel\hat{e}_1 + \Omega_\perp\hat{e}_2$, respectively, and these interact with a background shear flow $u = y e_3$.

the particle is given by $X = X e_1 + Y e_2 + Z e_3$ with respect to the orthonormal basis $\{e_1, e_2, e_3\}$ of the laboratory frame. These vectors are illustrated in figure 1.

Finally, we impose the far-field flow. Specifically, we are interested in the motion of the particle in the presence of a far-field shear Stokes flow with velocity field $u(x, y, z) = y e_3$, with coordinates x, y, z in the laboratory frame. The flow interacts with the particle; we derive the resulting governing equations of motion for the particle in Appendix A, and present the resulting equations below. The dynamics for the orientation of the swimmer frame is given in terms of the Euler angles (θ, ψ, ϕ), also defined formally in Appendix A.

The rotational dynamics is given by

$$\frac{d\theta}{dt} = \Omega_\perp \cos\psi + h_1(\theta, \phi; B, C), \tag{2.1a}$$

$$\frac{d\psi}{dt} = \Omega_\parallel - \Omega_\perp \frac{\cos\theta \sin\psi}{\sin\theta} + h_2(\theta, \phi; B, C, D), \tag{2.1b}$$

$$\frac{d\phi}{dt} = \Omega_\perp \frac{\sin\psi}{\sin\theta} + h_3(\theta, \phi; B, C), \tag{2.1c}$$

where the functions $h_i = f_i + g_i$ $(i = 1, 2, 3)$ capture the effects of the Stokes flow interacting with the swimmer. The f_i encode the rotational effects of the achiral aspects of the swimmer (and are the same as in Part 1). These functions are

$$f_1(\theta, \phi; B) := -\frac{B}{2}\cos\theta \sin\theta \sin 2\phi, \tag{2.2a}$$

$$f_2(\theta, \phi; B) := \frac{B}{2}\cos\theta \cos 2\phi, \tag{2.2b}$$

$$f_3(\phi; B) := \tfrac{1}{2}(1 - B\cos 2\phi), \tag{2.2c}$$

where B is the shape-capturing Bretherton parameter (Bretherton 1962), which typically satisfies $|B| < 1$ for all but the most elongated of bodies (Bretherton 1962; Singh, Koch & Stroock 2013).

979 A2-4

Parameter	Type of drift generated	Geometric cause
B	Rotational	Achiral 'aspect ratio'
C	Rotational component off symmetry axis	Chiral effects
D	Rotational component along symmetry axis	Chiral effects
β	Translational	Chiral effects
γ	Translational component off symmetry axis	Fore–aft asymmetry
δ	Translational component along symmetry axis	Fore–aft asymmetry

Table 1. Summary of the six parameters that characterise objects with hydrodynamic helicoidal symmetry.

The g_i encode the rotational effects of the chiral aspects of the swimmer, and were therefore not present in the spheroidal analysis of Part 1. These chiral functions are

$$g_1(\theta, \phi; C) := -\frac{C}{2} \sin\theta \cos 2\phi, \tag{2.3a}$$

$$g_2(\theta, \phi; C, D) := -\frac{C}{2} \cos^2\theta \sin 2\phi - \frac{D}{2} \sin^2\theta \sin 2\phi, \tag{2.3b}$$

$$g_3(\theta, \phi; C) := \frac{C}{2} \cos\theta \sin 2\phi. \tag{2.3c}$$

Here, C and D are chirality parameters, where C is sometimes referred to as the Ishimoto parameter (Ohmura *et al.* 2021). They represent rotational drift due to moments of chirality along the axis of helicoidal symmetry, as summarised in table 1. If the particle is spheroidal, then $C = D = 0$ and the governing equations for the rotational dynamics reduce to those in Part 1. For brevity, when referring to f_i and g_i, we will often suppress the explicit parameter dependence on B, C and D unless specifically relevant. The typical ranges of C and D are not well explored in the literature for different swimmers, with the notable exception of experimental measurements for bacterial swimmers, giving $C \approx 0.01$ (Jing *et al.* 2020; Ronteix *et al.* 2022; Zöttl *et al.* 2022). Given this, for reference we approximate plausible ranges of these parameters for a simple bacterial model using resistive force theory in Appendix B, which suggest $|C| \approx 0.01$ and $|D| \approx 0.5$. Since ψ decouples from the system (2.1)–(2.3) for passive swimmers (i.e. for $\Omega_\parallel = \Omega_\perp = 0$), and C appears to be small, one might assume that the effects of chirality are unimportant to Jeffery's orbits. We will show that this is not the case in general for the active swimmers that we consider. Therefore, we retain both C and D in our analysis, and we will see that this is important to capture comprehensively the nature of the emergent dynamics.

We now consider the governing equations for $X(t)$, the position of the swimmer in the laboratory frame. While the equivalent equations in Part 1 were fairly intuitive and straightforward to state, this was due to the intrinsic symmetry of spheroidal particles, which removed several of the more general contributions to translation. Since we now consider a more general class of objects, the translational dynamics in Part 2 feature additional contributions. We derive the resulting governing equations of motion in Appendix A, which are

$$\frac{\mathrm{d}X}{\mathrm{d}t} = V + Ye_3 - \beta \left(\hat{e}_2 \hat{e}_3^{\mathrm{T}} - \hat{e}_3 \hat{e}_2^{\mathrm{T}} \right) E^* \hat{e}_1 + \gamma E^* \hat{e}_1 + (\delta - \gamma) \left(\hat{e}_1^{\mathrm{T}} E^* \hat{e}_1 \right) \hat{e}_1. \tag{2.4}$$

We emphasise that V and $\hat{e}_i$ depend on the orientation of the object through the Euler angles (θ, ψ, ϕ), which evolve via (2.1)–(2.3). The additional terms in (2.4) not present in

Part 1 involve the rate of strain tensor $\boldsymbol{E}^*$, and three additional degrees of freedom encoded through the shape parameters β, γ and δ.

These shape parameters can be interpreted as measures of translational drift induced by the coupling between the shear-induced strain and asymmetries in the object shape. As summarised in table 1, β represents a measure of drift due to chirality of the object, and γ, δ represent measures of drift due to fore–aft asymmetry of the object. These additional translational terms arise in a similar manner to the additional terms (2.3) in the rotational dynamics. If the particle is spheroidal, then $\beta = \gamma = \delta = 0$ and the governing equations for the translational dynamics reduce to those in Part 1. In Appendix B, we estimate typical ranges of the shape parameters β, γ and δ using resistive force theory for a simple model bacterium swimmer.

The full dynamics comprising (2.1)–(2.4) governs the motion of any hydrodynamically helicoidal object in shear flow, by definition. That is, as discussed above, helicoidal objects are defined as objects that follow this dynamics, rather than by any necessary geometric properties. However, as we discuss below, there are important sufficient geometric conditions that give rise to hydrodynamic helicoidicity. In the hydrodynamic sense, the behaviour of helicoidal objects in shear flow is therefore fully characterised by the six parameters $B, C, D, \beta, \gamma, \delta$, summarised in table 1. This general class of shapes contains several subclasses of hydrodynamic symmetries, discussed extensively in Ishimoto (2020*a*). These subclasses include shapes that possess additional geometric symmetries, and are characterised mathematically by particular combinations of the six shape parameters vanishing.

We illustrate an example of a general hydrodynamically helicoidal body in figure 2(*a*), recalling that this includes (but is not limited to) objects possessing *n*-fold rotational symmetry along an axis for some integer $n \geqslant 4$. In particular, this allows the object to be chiral and to be free of any fore–aft symmetry constraints.

In figure 2(*b*), we illustrate four main hydrodynamic symmetry subcases of interest, giving examples of geometric symmetries that generate the specific subcases. An object that is geometrically symmetric with respect to a rotation of π around an axis perpendicular to the helicoidal symmetry axis has $C = D = \gamma = \delta = 0$; we describe an object satisfying these parameter constraints as possessing homochiral hydrodynamic symmetry, following the terminology employed in Ishimoto (2020*a*). A homochiral object does not experience any chirality-induced rotational drift. That is, from the governing equations (2.1)–(2.4), the effects of chirality in the dynamics of homochiral objects will manifest only through the drift velocity terms in the translational dynamics (2.4). Thus the rotational dynamics will remain as classic Jeffery orbits, while the translational dynamics will differ.

An object that is geometrically symmetric with respect to reflection in a plane normal to the axis of helicoidal symmetry has $\beta = \gamma = \delta = 0$; we describe an object satisfying these parameter constraints as possessing heterochiral hydrodynamic symmetry. A heterochiral object does not experience any chirality-induced translational drift. In particular, such an object always satisfies $\gamma = \delta = 0$. In contrast to homochiral objects, the effect of chirality in the dynamics of heterochiral objects will appear in the rotational drift terms in the rotational dynamics (2.1)–(2.3), resulting in chiral Jeffery orbits. These, in turn, will also influence the translational dynamics (2.4), which is coupled to the evolution of the object orientation. Given the geometric symmetries that generate homochiral or heterochiral objects, we describe an object in either subclass as possessing hydrodynamic fore–aft symmetry.
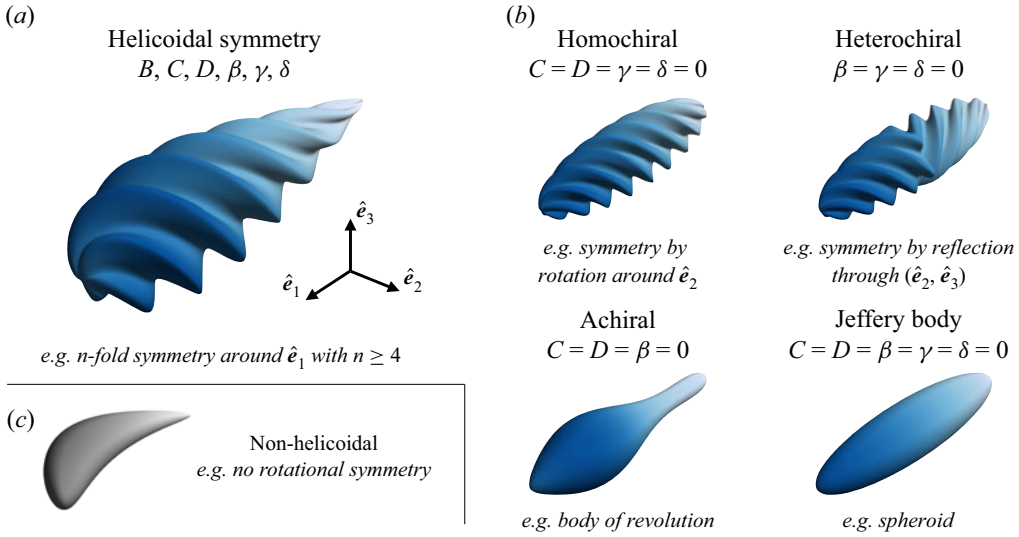
Figure 2. Examples of the class of shapes considered in Part 2. (*a*) The bodies that we investigate possess 'helicoidal' symmetry, which allows us to characterise their dynamics in shear flow with six parameters, $B, C, D, \beta, \gamma, \delta$. (*b*) We distinguish the specific subcases that we discuss in the main text: homochirality, heterochirality, achirality and Jeffery bodies, with this last class of objects following the simpler dynamics investigated in Part 1. Each category of shape is illustrated with an example particle possessing additional geometrical symmetries. (*c*) For comparison, we provide an example of a shape that does not possess helicoidal symmetry and therefore is not captured by our analysis.

An object that is geometrically symmetric with respect to continuous rotation around the helicoidal axis (i.e. a body of revolution) has $C = D = \beta = 0$; we describe an object satisfying these parameter constraints as possessing achiral hydrodynamic symmetry. Similar to the homochiral case, an achiral object does not experience any chirality-induced rotational drift. However, an achiral object will experience a different translational drift to a homochiral object in general.

Finally, any object with at least two of the geometric symmetries described above (e.g. a spheroid) has $C = D = \beta = \gamma = \delta = 0$; as noted in the Introduction, we describe an object satisfying these parameter constraints as a Jeffery body. We considered the simpler dynamics of these highly symmetric objects in Part 1.

More generally, in this study we investigate the emergent dynamics of the nonlinear, autonomous dynamical system defined by (2.1)–(2.4) for general helicoidal objects in shear flow. In the same manner as in Part 1, we consider the regime where the swimmer rotation rate is much larger than the external shear rate. This means that $|\boldsymbol{\Omega}| = |\Omega_\parallel \hat{\boldsymbol{e}}_1 + \Omega_\perp \hat{\boldsymbol{e}}_2|$ is large. Taking $\Omega_\parallel > 0$ without loss of generality, we consider the distinguished limit where $\Omega_\perp = O(\Omega_\parallel)$ with $\Omega_\parallel \gg 1$ (which will give the same information as taking $|\boldsymbol{\Omega}| \gg 1$ with $\alpha = O(1)$), and all other parameters are of $O(1)$. This asymptotic limit is distinguished in the sense that it is a general case from which the subcases $|\Omega_\perp| \gg \Omega_\parallel$ and $\Omega_\parallel \gg |\Omega_\perp|$ can be distilled as regular asymptotic sublimits of the results we derive.

3. Setting up the multiple scales analysis

We analyse the system (2.1)–(2.4) in the limit of rapid spinning. We animate the full dynamics of this system for various scenarios in supplementary movies 1–5 available at https://doi.org/10.1017/jfm.2023.924. We consider the distinguished limit $\Omega_\perp = O(\Omega_\parallel)$

with $\Omega_\parallel \gg 1$ (treating $\Omega_\parallel > 0$ without loss of generality). Given this, it is helpful to introduce the notation $\omega = O(1)$ such that

$$\Omega_\perp = \omega \Omega_\parallel, \tag{3.1}$$

and to formally consider the single asymptotic limit $\Omega_\parallel \gg 1$.

Our approach is similar to that in Part 1; we analyse the system (2.1)–(2.4) using the method of multiple scales in the limit of large $\Omega_\parallel$, with the goal of deriving effective equations that govern the emergent behaviour. Moreover, we will see that the leading-order system is equivalent to that of Part 1, so we are able to exploit the multiscale framework that we derived therein. The set-up for the multiple scales analysis is therefore equivalent to that in Part 1, and we repeat it here for convenience. We reintroduce T, the fast time scale, via

$$T = \left(\Omega_\perp^2 + \Omega_\parallel^2\right)^{1/2} t = \lambda \Omega_\parallel t, \tag{3.2}$$

where we use

$$\lambda := \sqrt{1 + \omega^2} \tag{3.3}$$

for notational convenience, and we refer to the original time scale t as the slow time scale. Treating the fast and slow time scales as independent and using (3.2), the time derivative becomes

$$\frac{\mathrm{d}}{\mathrm{d}t} \mapsto \lambda \Omega_\parallel \frac{\partial}{\partial T} + \frac{\partial}{\partial t}. \tag{3.4}$$

Under the time derivative mapping (3.4), the rotational dynamics system (2.1) is transformed to

$$\Omega_\parallel \lambda \frac{\partial \theta}{\partial T} + \frac{\partial \theta}{\partial t} = \Omega_\parallel \omega \cos \psi + h_1(\theta, \phi), \tag{3.5a}$$

$$\Omega_\parallel \lambda \frac{\partial \psi}{\partial T} + \frac{\partial \psi}{\partial t} = \Omega_\parallel \left(1 - \omega \frac{\cos \theta \sin \psi}{\sin \theta}\right) + h_2(\theta, \phi), \tag{3.5b}$$

$$\Omega_\parallel \lambda \frac{\partial \phi}{\partial T} + \frac{\partial \phi}{\partial t} = \Omega_\parallel \omega \frac{\sin \psi}{\sin \theta} + h_3(\theta, \phi), \tag{3.5c}$$

and the translational dynamics system (2.4) is transformed to

$$\lambda \Omega_\parallel \frac{\partial X}{\partial T} + \frac{\partial X}{\partial t} = V + Y e_3 - \beta \left(\hat{e}_2 \hat{e}_3^{\mathrm{T}} - \hat{e}_3 \hat{e}_2^{\mathrm{T}}\right) E^* \hat{e}_1 + (\delta - \gamma) \left(\hat{e}_1^{\mathrm{T}} E^* \hat{e}_1\right) \hat{e}_1 + \gamma E^* \hat{e}_1. \tag{3.6}$$

We expand each dependent variable as an asymptotic series in inverse powers of $\Omega_\parallel$, writing

$$\xi(T, t) \sim \xi_0(T, t) + \frac{1}{\Omega_\parallel} \xi_1(T, t) \quad \text{as } \Omega_\parallel \to \infty, \quad \text{for } \xi \in \{\phi, \theta, \psi, X, Y, Z\}. \tag{3.7}$$

Since the leading-order (fast) terms in (3.5) and (3.6) are $O(\Omega_\parallel)$, but the new chiral and asymmetric terms are all of $O(1)$, these new terms do not appear in the leading-order analysis. This means that the leading-order analysis and the adjoint solution used to derive the solvability conditions at next order are equivalent to those in Part 1, and we can therefore use directly the equivalent results therein. Consequently, we are fairly brief with the leading-order analysis and the derivation of the solvability conditions in the full analysis below, directing the interested reader to Part 1.

4. Deriving the emergent angular dynamics

4.1. *Leading-order analysis*

Using the asymptotic expansions (3.7) in the transformed governing equations (3.5), we obtain the leading-order (i.e. $O(\Omega_{\parallel})$) system

$$\lambda \frac{\partial \theta_0}{\partial T} = \omega \cos \psi_0, \tag{4.1a}$$

$$\lambda \frac{\partial \psi_0}{\partial T} = 1 - \omega \frac{\cos \theta_0 \sin \psi_0}{\sin \theta_0}, \tag{4.1b}$$

$$\lambda \frac{\partial \phi_0}{\partial T} = \omega \frac{\sin \psi_0}{\sin \theta_0}. \tag{4.1c}$$

We show in § 4.1 of Part 1 that the solution to the nonlinear system (4.1) is

$$\lambda \cos \theta_0 = \cos \bar{\vartheta} - \omega \sin \bar{\vartheta} \cos(T + \bar{\Psi}), \tag{4.2a}$$

$$\lambda \sin \theta_0 \sin \psi_0 = \omega \cos \bar{\vartheta} + \sin \bar{\vartheta} \cos(T + \bar{\Psi}), \tag{4.2b}$$

$$\tan \phi_0 = \frac{\omega \cos \bar{\varphi} \sin(T + \bar{\Psi}) + \sin \bar{\varphi}(\omega \cos \bar{\vartheta} \cos(T + \bar{\Psi}) + \sin \bar{\vartheta})}{\cos \bar{\varphi}(\omega \cos \bar{\vartheta} \cos(T + \bar{\Psi}) + \sin \bar{\vartheta}) - \omega \sin \bar{\varphi} \sin(T + \bar{\Psi})}, \tag{4.2c}$$

where $\bar{\vartheta} = \bar{\vartheta}(t)$, $\bar{\Psi} = \bar{\Psi}(t)$ and $\bar{\varphi} = \bar{\varphi}(t)$ are the three slow-time functions of integration that remain undetermined from our leading-order analysis. The goal of the next-order analysis in § 4.2 is to derive the governing equations satisfied by $\bar{\vartheta}$, $\bar{\Psi}$ and $\bar{\varphi}$. As in Part 1, one can think of $\bar{\vartheta}$ as controlling some emergent amplitude of oscillation, $\bar{\Psi}$ as controlling some emergent phase of oscillation, and $\bar{\varphi}$ as the emergent drift in yawing. We will also show later that $\bar{\vartheta}$ can be associated with θ, $\bar{\Psi}$ with ψ, and $\bar{\varphi}$ with ϕ.

Before proceeding, it will be helpful later to note the additional relationships

$$\sin \theta_0 \cos \psi_0 = - \sin \bar{\vartheta} \sin(T + \bar{\Psi}), \tag{4.2d}$$

$$\lambda^2 \sin^2 \theta_0 = (\omega \cos \bar{\vartheta} \cos(T + \bar{\Psi}) + \sin \bar{\vartheta})^2 + \omega^2 \sin^2(T + \bar{\Psi}), \tag{4.2e}$$

where the former follows from differentiating (4.2a) with respect to T and imposing (4.1a), and the latter follows from rearranging (4.2a).

4.2. *Next-order system*

Our remaining goal is to determine the governing equations satisfied by the slow-time functions $\bar{\vartheta}(t)$, $\bar{\Psi}(t)$ and $\bar{\varphi}(t)$. To do this, we must determine the solvability conditions required for the first-order correction (i.e. $O(1)$) terms in (3.5) after posing the asymptotic expansions (3.7). These $O(1)$ terms are

$$\lambda \frac{\partial \theta_1}{\partial T} + \omega \psi_1 \sin \psi_0 = h_1(\theta_0, \phi_0) - \frac{\partial \theta_0}{\partial t}, \tag{4.3a}$$

$$\lambda \frac{\partial \psi_1}{\partial T} - \omega \theta_1 \frac{\sin \psi_0}{\sin^2 \theta_0} + \omega \psi_1 \frac{\cos \theta_0 \cos \psi_0}{\sin \theta_0} = h_2(\theta_0, \phi_0) - \frac{\partial \psi_0}{\partial t}, \tag{4.3b}$$

$$\lambda \frac{\partial \phi_1}{\partial T} + \omega \theta_1 \frac{\cos \theta_0 \sin \psi_0}{\sin^2 \theta_0} - \omega \psi_1 \frac{\cos \psi_0}{\sin \theta_0} = h_3(\theta_0, \phi_0) - \frac{\partial \phi_0}{\partial t}, \tag{4.3c}$$

along with 2π-periodicity in T. The system (4.3) constitutes a non-autonomous linear coupled three-dimensional system for $(\theta_1, \psi_1, \phi_1)$ with an inhomogeneous forcing in terms of the leading-order solution.

To derive the required solvability conditions, we use the method of multiple scales for systems (see, for example, pp. 127–128 of Dalwadi (2014) or p. 22 of Dalwadi *et al.* (2018)). As detailed in §4.2 of Part 1, this entails taking the dot product of the vector solution to the homogeneous adjoint version of (4.3) with the vector right-hand side of (4.3), and averaging over one fast-time oscillation. We calculate the adjoint solution in §4.3 and Appendix D of Part 1; using this to apply the procedure outlined above yields the three solvability conditions

$$-\lambda \sin \bar{\vartheta}\, \frac{\mathrm{d}\bar{\vartheta}}{\mathrm{d}t} = \frac{\lambda \hat{B}}{2} \sin^2 \bar{\vartheta} \cos \bar{\vartheta} \sin 2\bar{\varphi}$$
$$+ \langle g_1(\omega \cos \theta_0 \sin \psi_0 - \sin \theta_0) + g_2 \omega \sin \theta_0 \cos \psi_0 \rangle, \quad (4.4a)$$

$$\lambda \sin^2 \bar{\vartheta}\, \frac{\mathrm{d}\bar{\Psi}}{\mathrm{d}t} = \frac{\lambda \hat{B}}{2} \sin^2 \bar{\vartheta} \cos \bar{\vartheta} \cos 2\bar{\varphi}$$
$$+ \langle g_1 \omega \cos \psi_0 + g_2 \sin \theta_0 (\sin \theta_0 - \omega \cos \theta_0 \sin \psi_0) \rangle, \quad (4.4b)$$

$$\cos \bar{\vartheta}\, \frac{\mathrm{d}\bar{\Psi}}{\mathrm{d}t} + \frac{\mathrm{d}\bar{\varphi}}{\mathrm{d}t} = \frac{1}{2}(1 - \hat{B} \sin^2 \bar{\vartheta} \cos 2\bar{\varphi}) + \langle g_2 \cos \theta_0 + g_3 \rangle, \quad (4.4c)$$

where we have used the results from §§4.2 and 4.3 of Part 1 to evaluate all the non-chiral terms (i.e. all terms not involving g_i), including the use of the effective Bretherton parameter that we derived in Part 1:

$$\hat{B} := \frac{(2 - \omega^2)B}{2(1 + \omega^2)}. \quad (4.5)$$

Additionally, we use the notation $\langle \cdot \rangle$ to denote the average of its argument over one fast-time oscillation, explicitly defining

$$\langle y \rangle = \frac{1}{2\pi} \int_0^{2\pi} y \,\mathrm{d}T. \quad (4.6)$$

Our remaining task is to evaluate the outstanding averages in the three solvability conditions (4.4), each of which involves the chiral contributions g_i defined in (2.3). We have explicit representations of the terms involving the trigonometric functions of θ_0 and ψ_0 through the leading-order solutions (4.2). The terms involving $\sin 2\phi_0$ and $\cos 2\phi_0$, which arise from the g_i defined in (2.2), require additional calculation. To derive expressions for these double-angle quantities, we first note

$$\lambda \sin \theta_0 \sin \phi_0 = \omega \cos \bar{\varphi} \sin \sigma + \sin \bar{\varphi}(\omega \cos \bar{\vartheta} \cos \sigma + \sin \bar{\vartheta}), \quad (4.7a)$$

$$\lambda \sin \theta_0 \cos \phi_0 = \cos \bar{\varphi}(\omega \cos \bar{\vartheta} \cos \sigma + \sin \bar{\vartheta}) - \omega \sin \bar{\varphi} \sin \sigma, \quad (4.7b)$$

using the shorthand $\sigma = T + \bar{\Psi}$. The expressions (4.7) are calculated via the identities $\tan \phi_0 = (\lambda \sin \theta_0 \sin \phi_0)/(\lambda \sin \theta_0 \cos \phi_0)$, and $\lambda^2 \sin^2 \theta_0 = (\lambda \sin \theta_0 \sin \phi_0)^2 + (\lambda \sin \theta_0 \cos \phi_0)^2$, the left-hand sides of which are defined in (4.2c) and (4.2e). Then, from

979 A2-10

the expressions of (4.7), appropriate double-angle formulae imply that

$$\lambda^2 \sin^2 \theta_0 \cos 2\phi_0 = \mathcal{C}(\sigma, t) \cos 2\bar{\varphi} - \mathcal{S}(\sigma, t) \sin 2\bar{\varphi}, \tag{4.8a}$$

$$\lambda^2 \sin^2 \theta_0 \sin 2\phi_0 = \mathcal{S}(\sigma, t) \cos 2\bar{\varphi} + \mathcal{C}(\sigma, t) \sin 2\bar{\varphi}, \tag{4.8b}$$

$$\mathcal{C}(\sigma, t) := (\omega \cos \bar{\vartheta} \cos \sigma + \sin \bar{\vartheta})^2 - \omega^2 \sin^2 \sigma, \tag{4.8c}$$

$$\mathcal{S}(\sigma, t) := 2\omega \sin \sigma (\omega \cos \bar{\vartheta} \cos \sigma + \sin \bar{\vartheta}). \tag{4.8d}$$

We can now simplify the remaining fast-time averages in the right-hand side of (4.4). We start by exploiting the parity of various expressions. Specifically, we use the evenness of $\cos \theta_0$, $\sin \theta_0 \sin \psi_0$, $\sin^2 \theta_0$ and $\mathcal{C}$ around $\sigma = \pi$ (from (4.2a), (4.2b), (4.2e) and (4.8c), respectively), and the oddness of $\sin \theta_0 \cos \psi_0$ and $\mathcal{S}$ around $\sigma = \pi$ (from (4.2d) and (4.8d), respectively). This allows us to write the fast-time averages in the right-hand side of (4.4) as

$$\langle g_1 (\omega \cos \theta_0 \sin \psi_0 - \sin \theta_0) + g_2 \omega \sin \theta_0 \cos \psi_0 \rangle$$

$$= -\frac{C}{2\lambda^2} \cos 2\bar{\varphi} \left\langle \mathcal{C} \left(\frac{\omega \cos \theta_0 \sin \psi_0}{\sin \theta_0} - 1 \right) + \frac{\mathcal{S}\omega \cos \psi_0}{\sin \theta_0} \right\rangle$$

$$+ \frac{C - D}{2\lambda^2} \cos 2\bar{\varphi} \langle \mathcal{S}\omega \sin \theta_0 \cos \psi_0 \rangle, \tag{4.9a}$$

$$\langle g_1 \omega \cos \psi_0 + g_2 \sin \theta_0 (\sin \theta_0 - \omega \cos \theta_0 \sin \psi_0) \rangle$$

$$= \frac{C}{2\lambda^2} \sin 2\bar{\varphi} \left\langle \mathcal{C} \left(\frac{\omega \cos \theta_0 \sin \psi_0}{\sin \theta_0} - 1 \right) + \frac{\mathcal{S}\omega \cos \psi_0}{\sin \theta_0} \right\rangle$$

$$+ \frac{D - C}{2\lambda^2} \sin 2\bar{\varphi} \langle \mathcal{C}(\omega \cos \theta_0 \sin \theta_0 \sin \psi_0 - \sin^2 \theta_0) \rangle, \tag{4.9b}$$

$$\langle g_2 \cos \theta_0 + g_3 \rangle = \frac{C - D}{2\lambda^2} \sin 2\bar{\varphi} \langle \mathcal{C} \cos \theta_0 \rangle. \tag{4.9c}$$

Using the leading-order solutions (4.2) with the definitions of $\mathcal{C}$ and $\mathcal{S}$ in (4.8c)–(4.8d), we may write the terms within the averages on the right-hand sides of (4.9) explicitly as

$$\mathcal{C} \left(\frac{\omega \cos \theta_0 \sin \psi_0}{\sin \theta_0} - 1 \right) + \frac{\mathcal{S}\omega \cos \psi_0}{\sin \theta_0} = -(1 + \omega^2) \sin \bar{\vartheta} (\sin \bar{\vartheta} + \omega \cos \bar{\vartheta} \cos \sigma),$$

$$\tag{4.10a}$$

$$\mathcal{S}\omega \sin \theta_0 \cos \psi_0 = -2\omega^2 \sin \bar{\vartheta} \sin^2 \sigma (\sin \bar{\vartheta} + \omega \cos \bar{\vartheta} \cos \sigma), \tag{4.10b}$$

$$\mathcal{C}(\omega \cos \theta_0 \sin \theta_0 \sin \psi_0 - \sin^2 \theta_0)$$

$$= \sin \bar{\vartheta} (\sin \bar{\vartheta} + \omega \cos \bar{\vartheta} \cos \sigma)(\omega^2 \sin^2 \sigma - (\sin \bar{\vartheta} + \omega \cos \bar{\vartheta} \cos \sigma)^2), \tag{4.10c}$$

$$\mathcal{C} \cos \theta_0 = \frac{\cos \bar{\vartheta} - \omega \sin \bar{\vartheta} \cos \sigma}{\lambda} ((\sin \bar{\vartheta} + \omega \cos \bar{\vartheta} \cos \sigma)^2 - \omega^2 \sin^2 \sigma). \tag{4.10d}$$

We can now calculate explicitly the averages of the right-hand sides of (4.10) over one fast-time oscillation, to deduce that

$$\left\langle \mathcal{C}\left(\frac{\omega \cos\theta_0 \sin\psi_0}{\sin\theta_0} - 1\right) + \frac{\mathcal{S}\omega \cos\psi_0}{\sin\theta_0}\right\rangle = -(1+\omega^2)\sin^2\bar{\vartheta}, \qquad (4.11a)$$

$$\langle \mathcal{S}\omega \sin\theta_0 \cos\psi_0\rangle = -\omega^2 \sin^2\bar{\vartheta}, \qquad (4.11b)$$

$$\langle \mathcal{C}(\omega \cos\theta_0 \sin\theta_0 \sin\psi_0 - \sin^2\theta_0)\rangle = -\frac{\sin^2\bar{\vartheta}}{2}(2\omega^2\cos^2\bar{\vartheta} + (2-\omega^2)\sin^2\bar{\vartheta}), \quad (4.11c)$$

$$\langle \mathcal{C}\cos\theta_0\rangle = \frac{2-3\omega^2}{2\lambda}\cos\bar{\vartheta}\sin^2\bar{\vartheta}. \qquad (4.11d)$$

Substituting (4.11) into (4.9), we deduce the following expressions for the averages of the chiral terms:

$$\langle g_1(\omega\cos\theta_0\sin\psi_0 - \sin\theta_0) + g_2\omega\sin\theta_0\cos\psi_0\rangle = \frac{C+\omega^2 D}{2\lambda^2}\cos 2\bar{\varphi}\sin^2\bar{\vartheta}, \quad (4.12a)$$

$$\langle g_1\omega\cos\psi_0 + g_2\sin\theta_0(\sin\theta_0 - \omega\cos\theta_0\sin\psi_0)\rangle$$
$$= -\frac{1}{2\lambda^2}\sin 2\bar{\varphi}\sin^2\bar{\vartheta}\left((C+\omega^2 D)\cos^2\bar{\vartheta} + \frac{3\omega^2 C + (2-\omega^2)D}{2}\sin^2\bar{\vartheta}\right), \quad (4.12b)$$

$$\langle g_2\cos\theta_0 + g_3\rangle = \frac{(C-D)(2-3\omega^2)}{4\lambda^2}\sin 2\bar{\varphi}\cos\bar{\vartheta}\sin^2\bar{\vartheta}. \qquad (4.12c)$$

Finally, to obtain the slow-time governing equations for $\bar{\vartheta}$, $\bar{\Psi}$ and $\bar{\varphi}$ that we have been seeking, we substitute the explicit averages (4.12) into the solvability conditions (4.4), and rearrange to obtain the reduced system

$$\frac{d\bar{\vartheta}}{dt} = -\frac{\hat{B}}{2}\sin\bar{\vartheta}\cos\bar{\vartheta}\sin 2\bar{\varphi} - \frac{\hat{C}}{2}\sin\bar{\vartheta}\cos 2\bar{\varphi}, \qquad (4.13a)$$

$$\frac{d\bar{\Psi}}{dt} = \frac{\hat{B}}{2}\cos\bar{\vartheta}\cos 2\bar{\varphi} - \frac{\hat{C}}{2}\cos^2\bar{\vartheta}\sin 2\bar{\varphi} - \frac{\hat{D}}{2}\sin^2\bar{\vartheta}\sin 2\bar{\varphi}, \qquad (4.13b)$$

$$\frac{d\bar{\varphi}}{dt} = \frac{1}{2}(1 - \hat{B}\cos 2\bar{\varphi}) + \frac{\hat{C}}{2}\cos\bar{\vartheta}\sin 2\bar{\varphi}, \qquad (4.13c)$$

where we define the effective chiral coefficients

$$\hat{C} := \frac{C+\omega^2 D}{(1+\omega^2)^{3/2}}, \quad \hat{D} := \frac{3\omega^2 C + (2-\omega^2)D}{2(1+\omega^2)^{3/2}}. \qquad (4.14a,b)$$

We illustrate these effective parameters in terms of ω in figure 3.

4.3. *Summary*

By comparison with the original angular dynamical system, defined in (2.1)–(2.3), we see that the emergent dynamics governed by (4.13) can be rewritten in terms of the combined
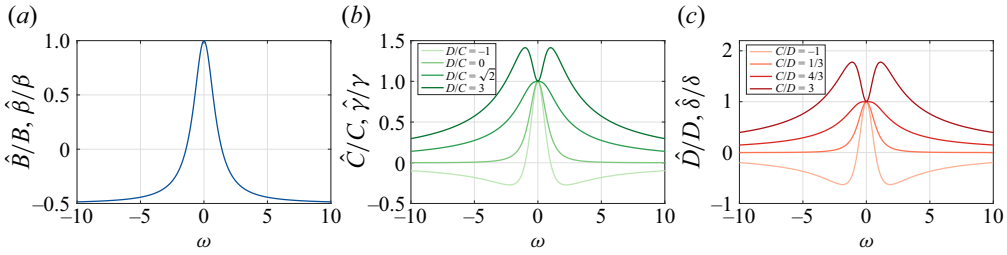
979 A2-12

Figure 3. The effective parameters $\hat{B}, \hat{C}, \hat{D}, \hat{\beta}, \hat{\gamma}, \hat{\delta}$ as functions of ω, normalised by their intrinsic equivalents. (a) $\hat{B}$ and $\hat{\beta}$ are functions only of ω, and exhibit the same dependence on ω following normalisation. (b,c) The remaining effective parameters are functions of three parameters. All are coupled to ω; the orientational shape parameters are also coupled to C and D, while the translational shape parameters are also coupled to γ and δ instead. We show selected curves for different parameter values. Several of the effective coefficients display non-trivial zeros as functions of ω. This suggests that specific activity-induced spinning can effectively eliminate certain parameters, and hence the associated physical interactions of an object with the flow.

achiral and chiral functions $h_i = f_i + g_i$ as

$$\frac{\mathrm{d}\bar{\vartheta}}{\mathrm{d}t} = h_1(\bar{\vartheta}, \bar{\varphi}; \hat{B}, \hat{C}), \quad \frac{\mathrm{d}\bar{\Psi}}{\mathrm{d}t} = h_2(\bar{\vartheta}, \bar{\varphi}; \hat{B}, \hat{C}, \hat{D}), \quad \frac{\mathrm{d}\bar{\varphi}}{\mathrm{d}t} = h_3(\bar{\vartheta}, \bar{\varphi}; \hat{B}, \hat{C}), \quad (4.15a\text{–}c)$$

where the effective Bretherton parameter $\hat{B}$ is defined in (4.5), and the effective chiral coefficients $\hat{C}$ and $\hat{D}$ are defined in (4.14a,b).

Therefore, similar to Part 1, the emergent dynamics for rapidly spinning chiral particles are governed by a system that has the same functional form as the original dynamical system without rapid spinning, but with modified coefficients (4.14a,b) that account for the effect of the spinning. As before, we can identify each slow-time function with an underlying variable: $\bar{\vartheta}$ with θ, $\bar{\Psi}$ with ψ, and ϕ with $\bar{\varphi}$. Since the slow terms in the original dynamical system represent the generalised Jeffery's equations for chiral particles, we can say that rapidly spinning chiral particles behave as particles with an effective chirality, as quantified through the effective coefficients (4.14a,b).

We explore the effect of rotation on the orientational dynamics in figure 4 and supplementary movies 1–4. In figure 4, we illustrate trajectories in the (ϕ, θ)-plane and set $D = 0$ for simplicity. In figures 4(a–c), we fix the Bretherton parameter $B = 0.7$ and vary the chirality parameter C in order to highlight the qualitative changes that chirality can induce. In figure 4(a), we set $C = 0$ and present standard Jeffery orbits for homochiral particles for the purpose of comparison, which are periodic as $|B| < 1$. Since this sublimit is a regular limit of the achiral analysis of Part 1, the trajectories shown in these plots are identical to those explored in Part 1. In figure 4(b), we increase the chirality parameter to $C = 0.7$, illustrating the trajectories of chiral objects. Here, the chirality breaks the periodicity of the slow-time generalised Jeffery trajectories for smaller values of ω, instead inducing a drift towards the pole $\theta = 0$. However, this periodicity-breaking effect appears to weaken for larger values of ω, when the effective chirality $\hat{C}$ of the object is reduced following (4.14a,b). In figure 4(c), we show trajectories for a strongly chiral object, increasing the chirality parameter to $C = 1.5$. Here, the chirality induced periodicity-breaking effect is stronger, with the notable appearance of attractive and repulsive points away from the poles at $\theta = 0, \pi$, and persists for larger values of ω before eventually leading to approximately periodic trajectories as ω increases further.
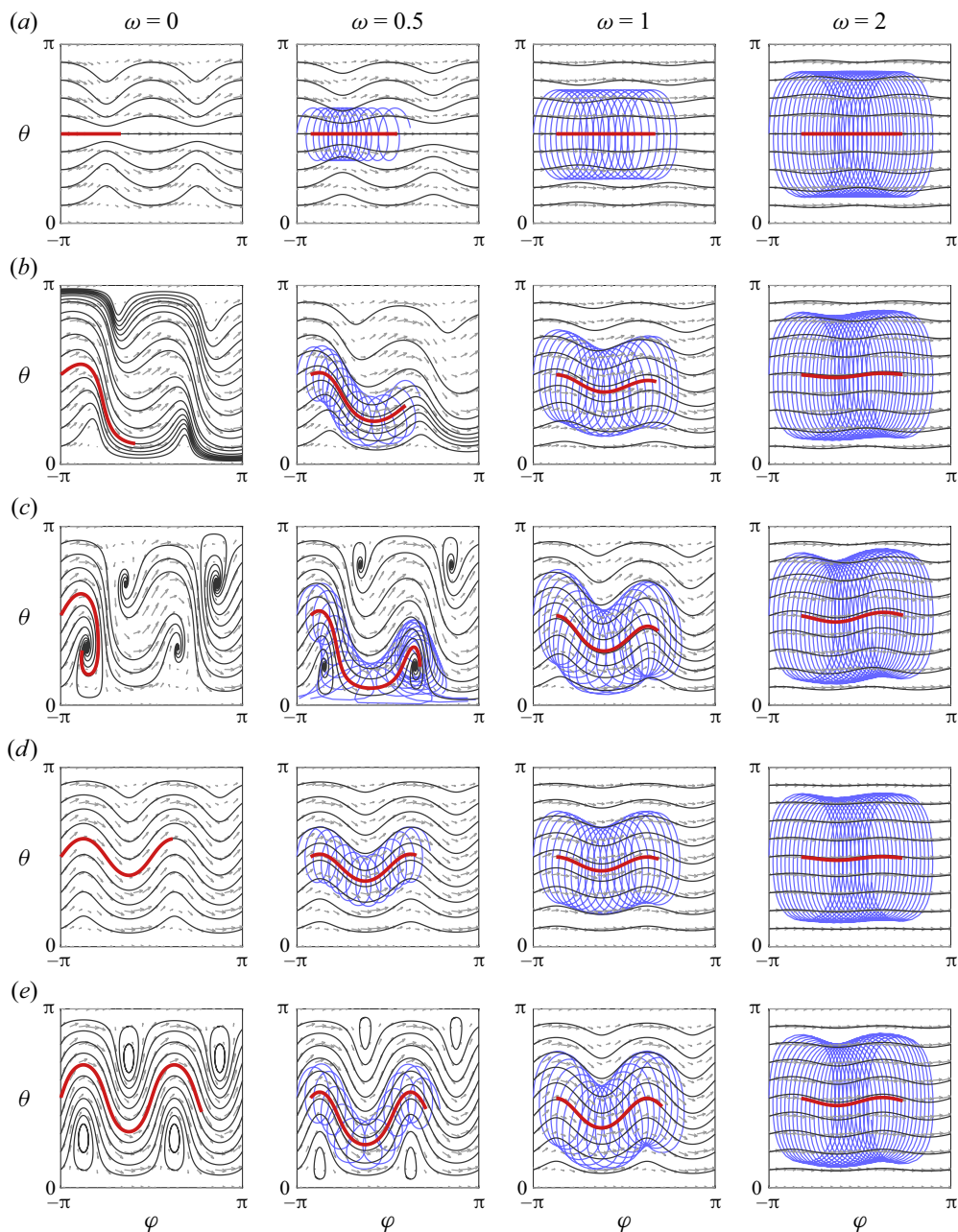
Figure 4. Exploring the orientational dynamics in the (ϕ, θ)-plane for various values of B, C and ω, with sample, rapidly oscillating full dynamics shown in blue for $\omega \neq 0$, and the corresponding averaged dynamics shown in red: (*a*) $(B, C) = (0.7, 0)$, (*b*) $(B, C) = (0.7, 0.7)$, (*c*) $(B, C) = (0.7, 1.5)$, (*d*) $(B, C) = (0, 0.7)$, and (*e*) $(B, C) = (0, 1.5)$. We use $D = 0$ and $(\theta, \phi) = (\pi/2, -\pi)$ at initial time throughout. For the blue lines, we also set $\Omega_{\parallel} = 10$ and $\Omega_{\perp} = 10\omega$. Dynamic versions of the full dynamics of the highlighted trajectories in (*b–e*) are given in supplementary movies 1–4.
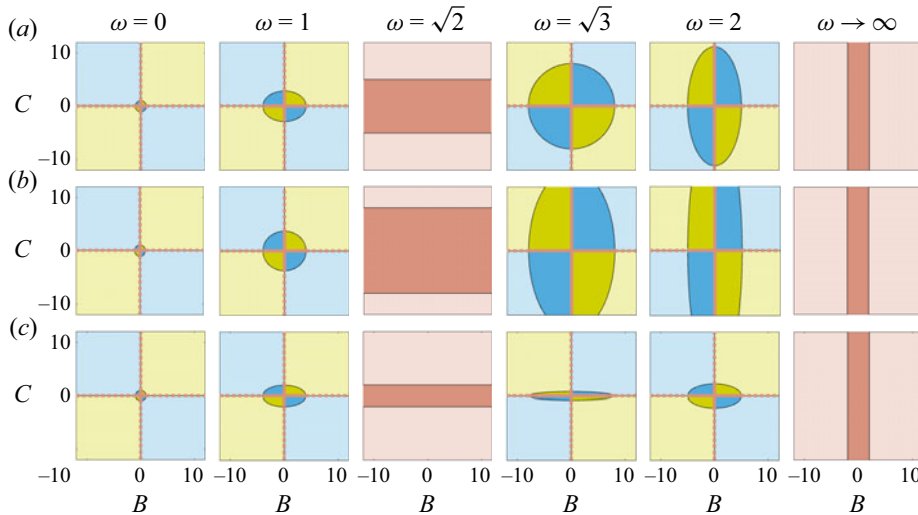
Figure 5. Schematic showing the qualitative nature of the orientational dynamics within the parameter space (B, C), for different values of ω. The darker regions within each ellipse indicate that trajectories drift towards a pole ($\theta = 0$ for the yellow region, $\theta = \pi$ for the blue region). Outside the ellipses, the pole solutions become repulsive points and non-trivial attractors exist. The lighter regions external to each ellipse indicate that these non-trivial attractors are in the northern (yellow) and southern (blue) hemispheres, respectively. The thicker red lines (solid and dashed) on the axes indicate periodic trajectories. Dashed lines indicate the existence of orbits that are not centred around one of the poles at $\theta = 0, \pi$. In the critical cases $\omega = \sqrt{2}$ and $\omega \to \infty$, all trajectories are orbits, so there exist only red regions. There is a distinction between orbits centred around a pole (darker red) and not centred around a pole (lighter red). Finally, the influence of the third shape parameter D is shown: (a) $D = 0$, (b) $D = 0.3$, and (c) $D = -0.3$.

In figures 4(d,e), we consider the effects of chirality on an object with vanishing Bretherton parameter, setting $B = 0$. In figure 4(d), we take $C = 0.7$, observing periodic trajectories whose behaviour is significantly more oscillatory in the θ variable than in the classical Jeffery orbits of figure 4(a). Further, $\theta = \pi/2$ is no longer a steady solution, which can also be seen by considering directly the contribution of the chiral function g_1 of (2.3a) in the governing equation (2.1a). As ω increases, we see a general reduction in these oscillations towards those of a sphere (with $B = C = 0$), as predicted by our explicit result for the effective chirality $\hat{C}$ in (4.14a,b). In figure 4(e), we consider a strongly chiral object by taking $C = 1.5$. In this case, the strongly chiral effects induce periodic orbits that, curiously, do not encircle the pole for smaller values of ω, instead orbiting around non-trivial fixed points in the (ϕ, θ)-plane. However, as ω increases and decreases $\hat{C}$, these orbits collapse, and the trajectories begin to approach those seen in figure 4(d) for smaller values of ω, as expected. The existence of periodic orbits that do not encircle the pole for larger values of C is due to the pole becoming a repulsive fixed point when $B^2 + C^2 > 1$ in the case of a passive object (Ishimoto 2020a,b), with non-trivial attractors emerging as a result of the bifurcation. In figure 5, we provide a visual characterisation of the qualitative behaviour of the solution space for the orientational dynamics in terms of the effective parameters $\hat{B}$ and $\hat{C}$.

Given these observations, it is of interest to note the limiting cases $\omega \to 0$ and $|\omega| \to \infty$. In the limit $\omega \to 0$, the effective chiral parameters remain the same, i.e. $\hat{C} \to C$ and $\hat{D} \to D$. That is, when spinning is rapid only around the axis of helicoidal symmetry, the effective shape of the chiral swimmer is unchanged; the rapid rotation does not impact

significantly the emergent angular dynamics. On the other hand, in the limit $|\omega| \to \infty$, the effective chiral parameters vanish, i.e. $\hat{C} \to 0$ and $\hat{D} \to 0$. That is, when rapid spinning only around an axis perpendicular to the axis of helicoidal symmetry, the rapid rotation causes the chiral swimmer to lose the effect of its chirality and for its orientation to evolve as though it were an achiral particle. This is because the coefficients C and D can be thought of as moments of chirality along the axis of helicoidal symmetry, and rapid rotation around an axis perpendicular to this will 'spread out' the chirality on average, reducing the effective moment to zero.

Additionally, we see that a chiral particle with $C = 0$ but $D \neq 0$ (or $D = 0$ but $C \neq 0$) can result in $\hat{C} \neq 0$ and $\hat{D} \neq 0$. That is, in certain cases with chiral particles, rapid spinning can generate effective terms that were not present in the original equations. Moreover, rapid spinning can either enhance or diminish the effects of chirality, depending on the specific values of C and D, and the relative rotation ratio ω.

A helpful way to interpret the effective chirality parameters $\hat{C}$ and $\hat{D}$, defined in (4.14*a,b*), is in terms of their relative sizes with respect to $\sqrt{C^2 + D^2}$, which can be considered a measure of the overall chirality of the object. To study this, it is helpful to introduce the parameter ζ, defined as the principal argument of the complex number

$$\exp(i\zeta) = \frac{C + iD}{|C + iD|}. \tag{4.16}$$

Therefore, the introduction of ζ collapses the two-dimensional parameter space (C, D) onto a single parameter via the complex unit circle. Then, utilising the relationship $\tan \alpha = \omega$, where α is the angle between the rotational and helicoidal axes, we can rewrite (4.14*a,b*) as

$$\frac{\hat{C}}{|C + iD|} = \cos \alpha (\cos^2 \alpha \cos \zeta + \sin^2 \alpha \sin \zeta), \tag{4.17a}$$

$$\frac{\hat{D}}{|C + iD|} = \frac{\cos \alpha}{2} (3 \sin^2 \alpha \cos \zeta + (2 \cos^2 \alpha - \sin^2 \alpha) \sin \zeta), \tag{4.17b}$$

which means that we can illustrate the left-hand sides of (4.17) in terms of just two parameters: α and ζ (see figures 6*a,b*). Through explicit calculation, it can also be shown that

$$\hat{C}^2 + \hat{D}^2 \leqslant C^2 + D^2, \tag{4.18}$$

which is illustrated in figure 6(*c*). Interpreting $\sqrt{C^2 + D^2}$ as a measure of the overall chirality of the object, we can deduce that rotation never increases the overall effective chirality. In fact, in general, rotation reduces the overall chirality, only leaving the overall chirality unchanged for $\alpha = 0$. While this reduction is a general property for the overall chirality, it is notable that (4.14*a,b*) implies that rotation can cause specific individual chirality parameters to increase. That is, rotation can cause $|\hat{C}| > |C|$ or $|\hat{D}| > |D|$, but the constraint (4.18) means that these cannot occur at the same time. Since C and D represent different aspects of chirality, we can interpret this as rotation allowing different aspects of chirality to be overemphasised or underemphasised, even though rotation reduces the overall chirality of the object.
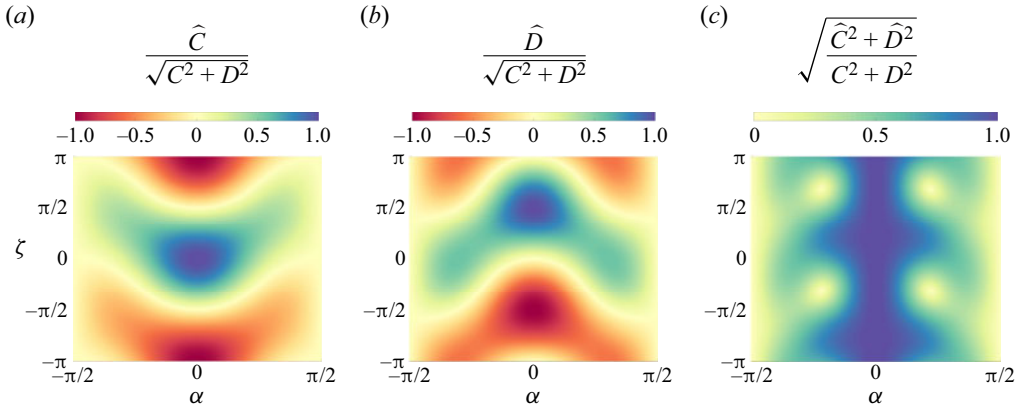
Figure 6. Representations of the scaled effective chiral coefficients: (a) $\hat{C}/\sqrt{C^2 + D^2} \in [-1, 1]$, (b) $\hat{D}/\sqrt{C^2 + D^2} \in [-1, 1]$, (c) $\sqrt{(\hat{C}^2 + \hat{D}^2)/(C^2 + D^2)} \in [0, 1]$. We define these quantities in (4.14*a,b*) and (4.17). Notably, the magnitude of each quantity is bounded above by 1, so we may conclude that the effect of rapid rotation is to reduce the effective overall chirality of an object.

5. Deriving the emergent translational dynamics

Using the asymptotic expansions (3.7) in the transformed governing equations (3.6), we obtain the trivial leading-order (i.e. $O(\Omega_\parallel)$) system

$$\frac{\partial X_0}{\partial T} = 0, \tag{5.1}$$

which tells us that $X_0 = X_0(t)$.

At next order (i.e. $O(1)$), we obtain the system

$$\lambda \frac{\partial X_1}{\partial T} + \frac{dX_0}{dt} = V + Y_0 e_3 - \beta \left(\hat{e}_2 \hat{e}_3^T - \hat{e}_3 \hat{e}_2^T \right) E^* \hat{e}_1 + \gamma E^* \hat{e}_1 + (\delta - \gamma) \left(\hat{e}_1^T E^* \hat{e}_1 \right) \hat{e}_1, \tag{5.2}$$

with 2π-periodicity in T, recalling that $V = V_1 \hat{e}_1 + V_2 \hat{e}_2 + V_3 \hat{e}_3$. The solvability condition that will give our emergent dynamics is obtained simply by averaging (5.2) over $T \in (0, 2\pi)$. Performing this averaging and imposing periodicity in T, (5.2) becomes

$$\frac{dX_0}{dt} = \left\langle V + Y_0 e_3 - \beta \left(\hat{e}_2 \hat{e}_3^T - \hat{e}_3 \hat{e}_2^T \right) E^* \hat{e}_1 + \gamma E^* \hat{e}_1 + (\delta - \gamma) \left(\hat{e}_1^T E^* \hat{e}_1 \right) \hat{e}_1 \right\rangle. \tag{5.3}$$

Some care needs to be taken in evaluating the right-hand side of (5.3), since the swimmer-frame basis vectors $\hat{e}_i$ are dependent on T through their dependence on the Euler angles, with the explicit dependence given in (A1). Importantly, since the leading-order analysis is the same between Parts 1 and 2, and the first two terms on the right-hand side of (5.3) are present in Part 1, we can use our results of § 4.5 of Part 1 to state immediately that

$$\langle V + Y_0 e_3 \rangle = \hat{V} \tilde{e}_1(\bar{\vartheta}, \bar{\varphi}) + Y_0 e_3, \tag{5.4}$$

where

$$\hat{V} := \frac{V_1 + \omega V_2}{\sqrt{1 + \omega^2}}, \tag{5.5}$$

and $\tilde{e}_1(\bar{\vartheta}, \bar{\varphi})$ can be considered equivalent to the (hatted) basis vector $\hat{e}_1$ in (A1), but with argument (θ, ϕ) replaced by $(\bar{\vartheta}, \bar{\varphi})$.

To calculate the remaining averages on the right-hand side of (5.3), we start by writing them in terms of the laboratory basis, using the swimmer-to-laboratory transformation (A1) and the definition of E^* (A5a,b). This yields

$$(\hat{e}_2\hat{e}_3^{\mathrm{T}} - \hat{e}_3\hat{e}_2^{\mathrm{T}})E^*\hat{e}_1 = \tfrac{1}{2}\big([s_\theta^2 c_{2\phi}]e_1 + [c_\theta s_\theta s_\phi]e_2 + [c_\theta s_\theta c_\phi]e_3\big), \tag{5.6a}$$

$$E^*\hat{e}_1 = -\tfrac{1}{2}(s_\theta c_\phi e_2 - s_\theta s_\phi e_3), \tag{5.6b}$$

$$(\hat{e}_1^{\mathrm{T}}E^*\hat{e}_1)\hat{e}_1 = -\tfrac{1}{2}\big([c_\theta s_\theta^2 s_{2\phi}]e_1 + [s_\theta^3 s_{2\phi}s_\phi]e_2 - [s_\theta^3 s_{2\phi}c_\phi]e_3\big), \tag{5.6c}$$

where we have used shorthand notation with c_θ, s_θ, c_ϕ, s_ϕ denoting $\cos\theta_0$, $\sin\theta_0$, $\cos\phi_0$, $\sin\phi_0$, and so on. We can then calculate the averages of (5.6) using the expressions (4.2) and (4.7)–(4.8) that we derived previously, to deduce that

$$\langle(\hat{e}_2\hat{e}_3^{\mathrm{T}} - \hat{e}_3\hat{e}_2^{\mathrm{T}})E^*\hat{e}_1\rangle = \frac{2-\omega^2}{4\lambda^2}\big([s_{\bar\vartheta}^2 c_{2\bar\varphi}]e_1 + [c_{\bar\vartheta}s_{\bar\vartheta}s_{\bar\varphi}]e_2 + [c_{\bar\vartheta}s_{\bar\vartheta}c_{\bar\varphi}]e_3\big)$$

$$= \frac{2-\omega^2}{2\lambda^2}\big(\tilde{e}_2\tilde{e}_3^{\mathrm{T}} - \tilde{e}_3\tilde{e}_2^{\mathrm{T}}\big)E^*\tilde{e}_1, \tag{5.7a}$$

$$\langle E^*\hat{e}_1\rangle = -\frac{1}{2\lambda}(s_{\bar\vartheta}c_{\bar\varphi}e_2 - s_{\bar\vartheta}s_{\bar\varphi}e_3) = \frac{E^*\tilde{e}_1}{\lambda}, \tag{5.7b}$$

$$\langle(\hat{e}_1^{\mathrm{T}}E^*\hat{e}_1)\hat{e}_1\rangle = -\frac{1}{4\lambda^3}\big[(2-3\omega^2)\{[c_{\bar\vartheta}s_{\bar\vartheta}^2 s_{2\bar\varphi}]e_1 + [s_{\bar\vartheta}^3 s_{2\bar\varphi}s_{\bar\varphi}]e_2$$

$$- [s_{\bar\vartheta}^3 s_{2\bar\varphi}c_{\bar\varphi}]e_3\} + 2\omega^2(s_{\bar\vartheta}c_{\bar\varphi}e_2 - s_{\bar\vartheta}s_{\bar\varphi}e_3)\big]$$

$$= \frac{2-3\omega^2}{2\lambda^3}\big(\tilde{e}_1^{\mathrm{T}}E^*\tilde{e}_1\big)\tilde{e}_1 + \frac{\omega^2}{\lambda^3}E^*\tilde{e}_1, \tag{5.7c}$$

where $\tilde{e}_i = \tilde{e}_i(\bar\vartheta, \bar\varphi)$ can be considered equivalent to their $\hat{e}_i$ (hatted) versions in (5.6) with arguments (θ_0, ϕ_0) replaced by $(\bar\vartheta, \bar\varphi)$.

Finally, substituting (5.4) and (5.7) into (5.3), we obtain our effective equation for the emergent translational dynamics:

$$\frac{\mathrm{d}X_0}{\mathrm{d}t} = \hat{V}\tilde{e}_1 + Y_0 e_3 - \hat{\beta}\big(\tilde{e}_2\tilde{e}_3^{\mathrm{T}} - \tilde{e}_3\tilde{e}_2^{\mathrm{T}}\big)E^*\tilde{e}_1 + \hat{\gamma}E^*\tilde{e}_1 + (\hat{\delta} - \hat{\gamma})\big(\tilde{e}_1^{\mathrm{T}}E^*\tilde{e}_1\big)\tilde{e}_1, \tag{5.8}$$

emphasising that $\tilde{e}_i$ are functions of the slow-time variables $\bar\vartheta$ and $\bar\varphi$, and that we have defined the effective coefficients

$$\hat{\beta} = \frac{(2-\omega^2)\beta}{2(1+\omega^2)}, \quad \hat{\gamma} = \frac{\gamma + \omega^2\delta}{(1+\omega^2)^{3/2}}, \quad \hat{\delta} = \frac{3\omega^2\gamma + (2-\omega^2)\delta}{2(1+\omega^2)^{3/2}}, \tag{5.9a–c}$$

and we illustrate these effective coefficients as functions of ω in figure 3. Therefore, we see that the effective translational equation (5.8) has the same functional form as the original equation (2.4), but with dependence on the fast-varying Euler angles switched to dependence on the slow-time functions that we derived in § 4, and modified coefficients (5.9a–c) that account systematically for the effect of the fast spinning. Therefore, we can say that rapidly spinning chiral particles are translated as particles with an effective chiral shape, as quantified through the effective shape coefficients defined in (5.9a–c). The excellent agreement between the complex full translational dynamics and the
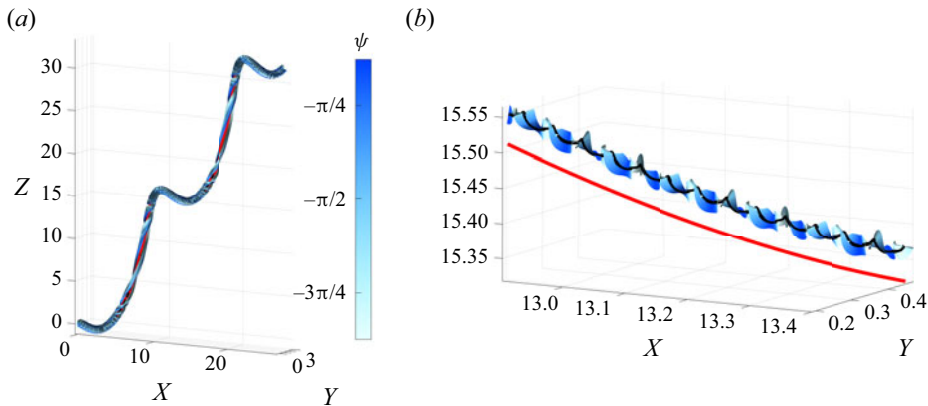
979 A2-18

Figure 7. Illustration of the agreement between the full spinning translational dynamics and the emergent system that we derive. (*a*) The predictions of the emergent dynamics are shown as a red curve, while the full dynamics is shown as a black line with attached ribbon, coloured according to the spin angle ψ of the object. Differences between the dynamics are barely visible at the resolution of this plot. (*b*) A portion of the trajectory in (*a*), showing the small (expected) discrepancy between the full and emergent solutions. Here, we have taken $\Omega_\parallel = \Omega_\perp = 100$, $B = 0.8$, $C = -0.3$, $D = -0.5$, $\beta = 0.01$, $\gamma = 0.3$, $\delta = -3$, $V_1 = 1$ and $V_2 = V_3 = 0.5$.

emergent dynamics predicted by (5.8) is illustrated on an example in figure 7, and we explore further the effect of varying the intrinsic shape parameters in figure 8.

Finally, we consider the limiting cases $\omega \to 0$ and $|\omega| \to \infty$. In the limit $\omega \to 0$, the effective coefficients are unchanged (i.e. $\hat{\beta} \to \beta$, $\hat{\gamma} \to \gamma$, $\hat{\delta} \to \delta$). That is, when the axis of rapid spinning coincides with the axis of helicoidal symmetry, the effective shape of the chiral swimmer is unchanged; the rapid rotation does not impact significantly the emergent translational dynamics. In contrast, in the limit $|\omega| \to \infty$ the effective coefficients are changed, with $\hat{\beta} \to -\beta/2$ and $\hat{\gamma}, \hat{\delta} \to 0$. We recall that the results of §4 state that the effective chirality coefficients also vanish in the same limit (i.e. $\hat{C}, \hat{D} \to 0$ as $|\omega| \to \infty$), and that passive homochiral objects satisfy $C = D = \gamma = \delta = 0$ (see figure 2). Therefore, we may conclude that when rapid spinning occurs around an axis perpendicular to the axis of helicoidal symmetry, a general active helicoidal swimmer will behave as though it is a passive homochiral swimmer. This can be interpreted intuitively by noting that a rapidly rotating swimmer with rotation axis perpendicular to its helicoidal axis can be thought of as exhibiting a geometric rotational symmetry of π around its rotation axis.

6. Results and conclusions

We investigated the emergent dynamics for a class of rapidly rotating active chiral particles with helicoidal symmetry, governed by the system (2.1)–(2.4). We considered the problem where rotation is fast compared to external shear rate, with the rotation axis pointing in a general direction, fixed in the swimmer frame. Formally, we analysed the distinguished asymptotic limit $\Omega_\parallel, \Omega_\perp \gg 1$ with $\omega = \Omega_\perp/\Omega_\parallel = O(1)$, noting that these quantities are related to the angle of the rotation axis from the symmetry axis α via $\tan\alpha = \omega$. From our analysis in §§4 and 5, we found that, somewhat remarkably, the effect of rapid rotation can be incorporated readily into generalised Jeffery's equations with effective coefficients (4.15*a–c*), (5.8), as long as the emergent dynamics is defined in terms of appropriately transformed variables. This means that rapid rotation modifies the emergent dynamics only through changes in the effective shape parameters. That is, an active, rapidly
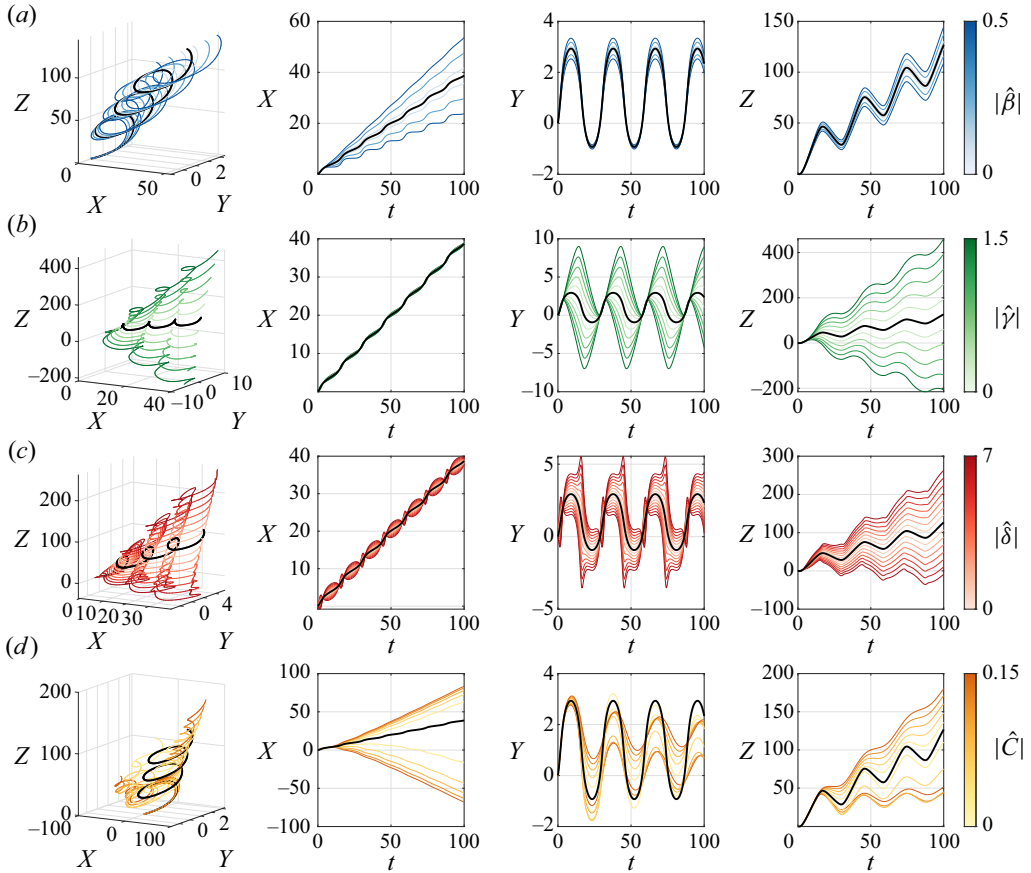
Figure 8. Exploring the influence of the effective geometric parameters $\hat{\beta}$, $\hat{\gamma}$, $\hat{\delta}$ and $\hat{C}$ on the emergent translational dynamics. In each panel, we vary each effective parameter independently from $(\hat{\beta}, \hat{\gamma}, \hat{\delta}, \hat{C}) = (0, 0, 0, 0)$, highlighting the distinct role that each parameter plays in determining the emergent translational dynamics. In each column, we show three-dimensional trajectories and traces of laboratory-frame coordinates over time. Throughout, we use initial conditions $X = 0$ and $(\theta, \phi, \psi) = (\pi/3, \pi/6, 2\pi/3)$.

spinning object exhibits the effective hydrodynamic shape of a (generally) differently shaped, non-spinning object. Moreover, our results characterise and quantify the specific hydrodynamic relationship between passive and rapidly spinning objects through explicit calculation of these effective parameters, each in terms of relevant original parameters and as a nonlinear function of $\omega = \tan \alpha$.

Our analysis allows us to interpret physically the effect of rapid rotation on the emergent trajectories. As we discuss in more detail below, the effect of rotation off the helicoidal axis ($\Omega_\perp$) is more important to the emergent dynamics than rotation on the helicoidal axis ($\Omega_\parallel$). Moreover, the broad effect of increasing α, the angle between the axes of rotation and symmetry, is to reduce the overall effective chirality of the effective hydrodynamic shape. Importantly, however, moving the rotation axis away from the symmetry axis can overemphasise and underemphasise different aspects of chirality. This includes chiral aspects that do not affect significantly the dynamics of passive chiral objects in flow; as described below, our results show that rapid rotation can cause these aspects to become much more important for active helicoidal particles in flow.

979 A2-20

For the spheroidal objects of Part 1, there is only one quantity, the Bretherton parameter B, that characterises hydrodynamic interactions with the object. In contrast, as summarised in table 1, there are six shape parameters that specify the hydrodynamic interaction for a general helicoidal shape (Ishimoto 2020*a*). Three of these – B, C and D – arise in the orientational dynamics, and the other three – β, γ and δ – arise in the translational dynamics. As illustrated in figure 2, for a hydrodynamically achiral particle, we have $C = D = \beta = 0$, and for a particle with hydrodynamic fore–aft symmetry (i.e. either homochiral or heterochiral), we have $\gamma = \delta = 0$. We note that spheroids satisfy both of these constraints. Through our multiscale analysis, we have derived explicit forms for the effective versions of these parameters in (4.5), (4.14*a,b*) and (5.9*a–c*) (denoted with hats), which quantify and account systematically for the effects of rapid rotation in the system.

Notably, the presence of chirality and fore–aft asymmetry does not change explicitly the effective Bretherton parameter $\hat{B}$, defined in (4.5), from its equivalent expression in Part 1. However, the inclusion of these additional effects does impact upon the overall orientational dynamics of the emergent system (4.15*a–c*), since they introduce additional terms involving $\hat{C}$ and $\hat{D}$ (defined in (4.14*a,b*)) into the overall system. These two chirality parameters are the effective versions of C and D, respectively. Notably, each of $\hat{C}$ and $\hat{D}$ depends on both C and D, and we show that $\hat{C}^2 + \hat{D}^2 \leqslant C^2 + D^2$ in §4.2.1. By interpreting $C^2 + D^2$ as a measure of the overall hydrodynamic chirality of an object for its orientational dynamics, the effect of rotation is therefore to reduce the overall effective chirality of the object.

Interestingly, however, rotation can cause $\hat{C} > C$ or $\hat{D} > D$ (though, from the constraint above, not both at the same time). Since C and D reflect the moment of chirality along the helicoidal axis, this means that rapid rotation can enhance certain hydrodynamic aspects of chirality while reducing the overall hydrodynamic chirality of the object. Moreover, we note that the object 'spin' $\psi(t)$ essentially decouples from the remaining variables in the full passive system (obtained by setting $\Omega_\parallel = \Omega_\perp = 0$ in (2.1)). Since D appears only in (2.1*b*), the equation for ψ, this parameter is generally not important for the overall (θ, ϕ) dynamics of the system, often the key observable dynamical outputs. However, our analytic results in (4.14*a,b*) show that rotation can cause D to affect significantly the effective coefficient $\hat{C}$, which is important for the overall slow-time dynamics. This means that D can be very important for the dynamics of rotating bodies, but unimportant for passive bodies. This effect could also explain why resistive force theory calculations give values for C slightly smaller than experimental estimates (Jing *et al.* 2020; Zöttl *et al.* 2022). That is, values of C calculated theoretically for simple bacterium models can be fairly small, in contrast to D (see e.g. estimates using resistive force theory calculations in Appendix B). However, since the effective Ishimoto parameter $\hat{C}$ can be enhanced by D in the presence of rotation, the (observed) effective Ishimoto parameter $\hat{C}$ for spinning objects can be larger than for its passive equivalent C.

An interesting implication of our results is that there are specific rotation rates and relationships between chirality parameters that cause both effective chirality parameters to vanish. Specifically, from (4.14*a,b*), we see that a rotation axis satisfying $\tan^2 \alpha = 2/3$ with chirality parameters satisfying $3C + 2D = 0$ will result in $\hat{C} = \hat{D} = 0$. This will result in the rotating object behaving hydrodynamically as an achiral object. While this requirement may be overly prescriptive to be observed in nature, it may be feasible to achieve for designed artificial swimmers. We note that this procedure is likely to involve a challenging optimisation process over the space of swimmer shapes, since the problem of finding a

shape that satisfies specific coefficients is an inverse problem. This is in contrast to the less complex 'forward' problem of calculating the shape coefficients from a given shape. It would be interesting in the future to solve the inverse problem of calculating object shapes that satisfy these constraints. Swimmers with these properties would behave as chiral objects when passive, and as achiral objects when rotating rapidly with $\tan^2 \alpha = 2/3$. In addition, since a critical rotation axis satisfying $\tan^2 \alpha = 2$ causes the effective Bretherton parameter $\hat{B}$ to vanish (so that the object is hydrodynamically equivalent to a sphere if it is achiral), it is not possible in general to prescribe a single critical rotation axis that causes $\hat{B}$, $\hat{C}$ and $\hat{D}$ to vanish simultaneously.

The implications of our emergent translational dynamics (5.8) have direct equivalence with the interpretation given above. This is because the effective shape parameters for translational dynamics in (5.9*a–c*) are analogous to their orientational counterparts in (4.5) and (4.14*a,b*). That is, the functional dependence on the rotation angle $\alpha = \arctan \omega$ of the effective shape parameter $\hat{\beta}$ in (5.9*a–c*) is the same as that of the effective Bretherton parameter $\hat{B}$ in (4.5). Similarly, $\hat{\gamma}$ and $\hat{\delta}$ in (5.9*a–c*) have the same functional dependence on α as $\hat{C}$ and $\hat{D}$, respectively, in (4.14*a,b*). Therefore, all of our conclusions above for $\hat{B}$, $\hat{C}$ and $\hat{D}$ in the orientational dynamics also hold for $\hat{\beta}$, $\hat{\gamma}$ and $\hat{\delta}$, respectively, in the translational dynamics. Perhaps interestingly, as noted above, β arises from chiral effects, and γ, δ can arise from a lack of fore–aft symmetry of the object. Therefore, the implications for $\hat{B}$, the effective Bretherton parameter for rotation (here for chiral particles, and in Part 1 for spheroidal particles), can be extended to the effective translation coefficient $\hat{\beta}$. Similarly, the implications for the effective chirality coefficients for rotation $\hat{C}$ and $\hat{D}$ can be extended to the effective translation coefficients $\hat{\gamma}$ and $\hat{\delta}$. Therefore, by direct analogy with the results highlighted above and in Part 1, specific rotation rates and parameter dependencies can remove hydrodynamic chiral and fore–aft asymmetry effects in the effective translational dynamics.

7. Discussion

This study is the second in a two-part series, in which we have explored the emergent dynamics of three-dimensional, rapidly spinning, helicoidal objects in shear Stokes flow. In Part 2, we have explored the behaviours of completely general helicoidal objects, generalising our results from the spheroidal swimmer shape that we imposed in Part 1. We have used the method of multiple scales for systems to systematically derive effective governing equations for the object dynamics. We have found that when written in terms of appropriately transformed variables, the emergent equations are the generalised Jeffery's equations for passive chiral objects derived in Ishimoto (2020*a*), with appropriately modified hydrodynamic coefficients that account for the effects of rotation.

Our multiscale approach was vital in calculating these modified parameters explicitly. We used the method of multiple scales for systems (e.g. see pp. 127–128 of Dalwadi (2014) or p. 22 of Dalwadi *et al.* (2018)) to derive systematically the appropriate emergent equations, which involved solving a three-dimensional nonlinear leading-order system, and a non-self-adjoint problem at next order. The analytic derivation of the effective parameters allowed us to interrogate the general effect of rapid rotation on the emergent dynamics of helicoidal objects in shear flow. We showed that rotation along the helicoidal axis had little effect on the emergent dynamics. However, rotation off this axis had a more significant effect. Broadly, off-axis rotation reduces the overall magnitude of the effective parameters for both achiral and chiral objects. More specifically, the general effect of

increasing off-axis rotation is to bring the effective aspect ratio of objects closer to unity through the reduction in magnitude of the effective Bretherton parameter $\hat{B}$. For chiral objects, the general effect of increasing off-axis rotation is to reduce the overall effect of chirality.

A curious aspect of our analysis is the nature of the equivalence between the effective equations that we derive and the generalised Jeffery's equations for inert particles. Specifically, this equivalence is explicitly evident only when the slow-time variables that arise from our analysis are written in terms of suitably transformed variables. Although the appropriate definitions for these slow-time variables are related to the 'average' position of the object, their specific choice is not immediately apparent when they first arise in the analysis. The choice that we make in using specifically $\bar{\vartheta}(t)$, $\bar{\Psi}(t)$ and $\bar{\varphi}(t)$ in (4.2) appears to be justified only once we finally derive the emergent equations (4.15*a–c*). This is in contrast to recent applications of multiscale analysis to two-dimensional swimming problems (Walker *et al.* 2022*a*,*b*), where the equivalence between slow- and fast-time variables is more apparent from the start.

A natural question to ask is whether our results can be extended to consider several swimmers. In general, the consideration of multiple swimmers would be significantly more challenging, due partly to the difficulties in calculating explicit hydrodynamic tensors that account for the orientation of several swimmers simultaneously. A specific sublimit in which it may be possible to adapt our results is the limit of dilute suspensions, where swimmers are well separated and swimmer–swimmer interactions are rare. In this case, it may be possible to extend our results to estimate probability distributions for organism orientation as a function of local shear rate, though this remains a subject for future work. Additionally, it may be possible to generate effective equations by applying our methodology to point-particle models for the alignment of particles via hydrodynamic interactions (Katuri *et al.* 2022).

To conclude, over this two-part study, we have investigated the behaviours of rapidly spinning, three-dimensional, helicoidal objects in shear flow. We have shown that the emergent orientational and translational dynamics can be described by the dynamics of passive, differently shaped objects in appropriately transformed variables. Moreover, we have calculated analytic representations of the effective parameters that encode the effective hydrodynamic shape of these objects. In other words, our systematic analysis has highlighted that the angular behaviours of such spinning objects can be described by generalisations of Jeffery's orbits for effective passive objects, so that this study serves to complement the works of Bretherton (1962), Brenner (1964*b*) and Ishimoto (2020*a*,*b*) by broadening further the scope of Jeffery's classical study of objects in slow flow (Jeffery 1922).

M.P. Dalwadi, C. Moreau, E.A. Gaffney, B.J. Walker and K. Ishimoto

Author ORCIDs.

- M.P. Dalwadi https://orcid.org/0000-0001-5017-2116;
- C. Moreau https://orcid.org/0000-0002-8557-1149;
- E.A. Gaffney https://orcid.org/0000-0002-6888-4362;
- B.J. Walker https://orcid.org/0000-0003-0853-267X;
- K. Ishimoto https://orcid.org/0000-0003-1900-7643.

Appendix A. Deriving the equations of motion

In this appendix, we derive the equations of motion for a self-propelled helicoidal swimmer in a simple shear, introduced in § 2.

A.1. *Kinematics*

We take the origin of the swimmer frame $X = Xe_1 + Ye_2 + Ze_3$ to be the centre of hydrodynamic mobility of the swimmer. Therefore, X lies on $\hat{e}_1$ (Kim & Karrila 1991). To specify the angular dynamics, we introduce the Euler angles, for which we use the *xyx* convention, with $\phi \in [0, 2\pi]$, $\theta \in [0, \pi]$ and $\psi \in [0, 2\pi]$, noting that we interpret ϕ and ψ modulo 2π. In terms of the swimmer-fixed and laboratory frames, the transformation between basis vectors is given by

$$\begin{pmatrix} \hat{e}_1 \\ \hat{e}_2 \\ \hat{e}_3 \end{pmatrix} = \begin{pmatrix} c_\theta & s_\phi s_\theta & -c_\phi s_\theta \\ s_\psi s_\theta & c_\phi c_\psi - s_\phi c_\theta s_\psi & s_\phi c_\psi + c_\phi c_\theta s_\psi \\ c_\psi s_\theta & -c_\phi s_\psi - s_\phi c_\theta c_\psi & -s_\phi s_\psi + c_\phi c_\theta c_\psi \end{pmatrix} \begin{pmatrix} e_1 \\ e_2 \\ e_3 \end{pmatrix}, \qquad (A1)$$

as illustrated in Appendix A of Part 1, with c_θ, s_θ denoting $\cos\theta$, $\sin\theta$, and similarly for other angles.

Further, the Euler angle transformation also gives the relation between the angular velocity of the swimmer frame in the presence of flow, denoted $\boldsymbol{\Omega}^f$, and the time derivatives of the Euler angles via

$$\boldsymbol{\Omega}^f = \dot{\phi}e_1 + \dot{\theta}e_2' + \dot{\psi}\hat{e}_1 = \sum \hat{\Omega}_p^f \hat{e}_p, \qquad (A2)$$

which simplifies to

$$\begin{pmatrix} \dot{\theta} \\ \dot{\psi} \\ \dot{\phi} \end{pmatrix} = \begin{pmatrix} 0 & c_\psi & -s_\psi \\ 1 & -s_\psi c_\theta/s_\theta & -c_\psi c_\theta/s_\theta \\ 0 & s_\psi/s_\theta & c_\psi/s_\theta \end{pmatrix} \begin{pmatrix} \hat{\Omega}_1^f \\ \hat{\Omega}_2^f \\ \hat{\Omega}_3^f \end{pmatrix}. \qquad (A3)$$

Writing $x = xe_1 + ye_2 + ze_3$ for the position of a general point in the domain, we consider the shear flow

$$u(x) = ye_3 = Ye_3 + (y - Y)e_3, \qquad (A4)$$

where we have decomposed the flow into its contribution at the origin of the swimmer frame, defining $V^* = Ye_3$, and a disturbance $(y - Y)e_3$ relative to this. The associated rate of strain and fluid angular velocity are given by

$$E^* = \tfrac{1}{2}\left(\nabla u + (\nabla u)^{\mathrm{T}}\right) = \tfrac{1}{2}\left(e_2 e_3^{\mathrm{T}} + e_3 e_2^{\mathrm{T}}\right), \quad \boldsymbol{\Omega}^* = \tfrac{1}{2}\nabla \wedge u = \tfrac{1}{2}e_1. \qquad (A5a,b)$$

979 A2-24

A.2. *Mechanics*

The grand mobility tensor formulation of Kim & Karrila (1991), with no external flow and viscosity non-dimensionalised to unity, gives the general relations

$$\begin{pmatrix} -V \\ -\boldsymbol{\Omega} \\ S^* \end{pmatrix} = \begin{pmatrix} a & \tilde{b} & \tilde{g} \\ b & c & \tilde{h} \\ g & h & m \end{pmatrix} \begin{pmatrix} F \\ T \\ 0 \end{pmatrix}. \tag{A6}$$

The block entries of the grand mobility tensor relate the force F and torque T generated by the self-propulsion mechanism to the velocity, angular velocity and stresslet of the particle in a quiescent field, which we denote by V, $\boldsymbol{\Omega}$ and S^*, respectively.

Furthermore, noting that F and T are assumed to be invariant on imposing the external shear flow, we have the analogous relation

$$\begin{pmatrix} V^* - V^f \\ \boldsymbol{\Omega}^* - \boldsymbol{\Omega}^f \\ S^f \end{pmatrix} = \begin{pmatrix} a & \tilde{b} & \tilde{g} \\ b & c & \tilde{h} \\ g & h & m \end{pmatrix} \begin{pmatrix} F \\ T \\ E^* \end{pmatrix}, \tag{A7}$$

where we recall that $V^* = Ye_3$ is the undisturbed velocity of the external flow at the origin of the swimmer frame, $\boldsymbol{\Omega}^*$ and E^* are given by (A5*a,b*), and V^f, $\boldsymbol{\Omega}^f$ and S^f are the velocity, angular velocity and stresslet of the particle in the shear flow, respectively.

Using (A6) to eliminate F and T from (A7), we can rewrite the force F and torque T in terms of the swimming velocities V and $\boldsymbol{\Omega}$ to obtain the translational velocity expressions

$$V^f = V + Ye_3 - \tilde{g}E^*, \quad (\tilde{g}E^*)_i = \tilde{g}_{ipq}E^*_{pq}, \quad \tilde{g}_{iqp} = \tilde{g}_{ipq}, \tag{A8a,b}$$

and the rotational velocity expressions

$$\boldsymbol{\Omega}^f = \boldsymbol{\Omega} + \boldsymbol{\Omega}^* - \tilde{h}E^*, \quad (\tilde{h}E^*)_i = \tilde{h}_{ipq}E^*_{pq}, \quad \tilde{h}_{iqp} = \tilde{h}_{ipq}. \tag{A9a,b}$$

The expressions for $\tilde{g}E^*$ and $\tilde{h}E^*$ are derived in Ishimoto (2020*a,b*) for helicoidal objects. Using these expressions, we deduce that

$$V^f = V + Ye_3 - \beta \left(\hat{e}_2 \hat{e}_3^{\mathrm{T}} - \hat{e}_3 \hat{e}_2^{\mathrm{T}} \right) E^* \hat{e}_1 + \gamma E^* \hat{e}_1 + (\delta - \gamma) \left(\hat{e}_1^{\mathrm{T}} E^* \hat{e}_1 \right) \hat{e}_1, \tag{A10}$$

where β is a shape parameter corresponding to chiral effects (which vanishes for an achiral particle), and γ, δ are shape parameters corresponding to fore–aft asymmetry effects (which vanish for a particle with hydrodynamic fore–aft symmetry), and

$$\boldsymbol{\Omega}^f = \boldsymbol{\Omega} + \boldsymbol{\Omega}^* - B \left(\hat{e}_2 \hat{e}_3^{\mathrm{T}} - \hat{e}_3 \hat{e}_2^{\mathrm{T}} \right) E^* \hat{e}_1 + C E^* \hat{e}_1 + (D - C) \left(\hat{e}_1^{\mathrm{T}} E^* \hat{e}_1 \right) \hat{e}_1, \tag{A11}$$

where B and C are the Bretherton and Ishimoto parameters, and D is an additional shape parameter generated by the chirality of the object.

Substituting (A11) into (A3) and using the frame transformation (A1) yields the angular dynamics given in (2.1)–(2.3). Recalling that $\mathrm{d}X/\mathrm{d}t = V^f$ and using (A10) yields the translational dynamics given in (2.4).

Appendix B. Estimation of shape parameters for a model bacterium

In this appendix, we estimate values of the shape parameters B, C, D, β, γ and δ for a simple model bacterium used in a previous study (Ishimoto 2020*a*). This simple model consists of a rigid spheroidal cell body (with semi-axes c, a, a) and helicoidal flagellum
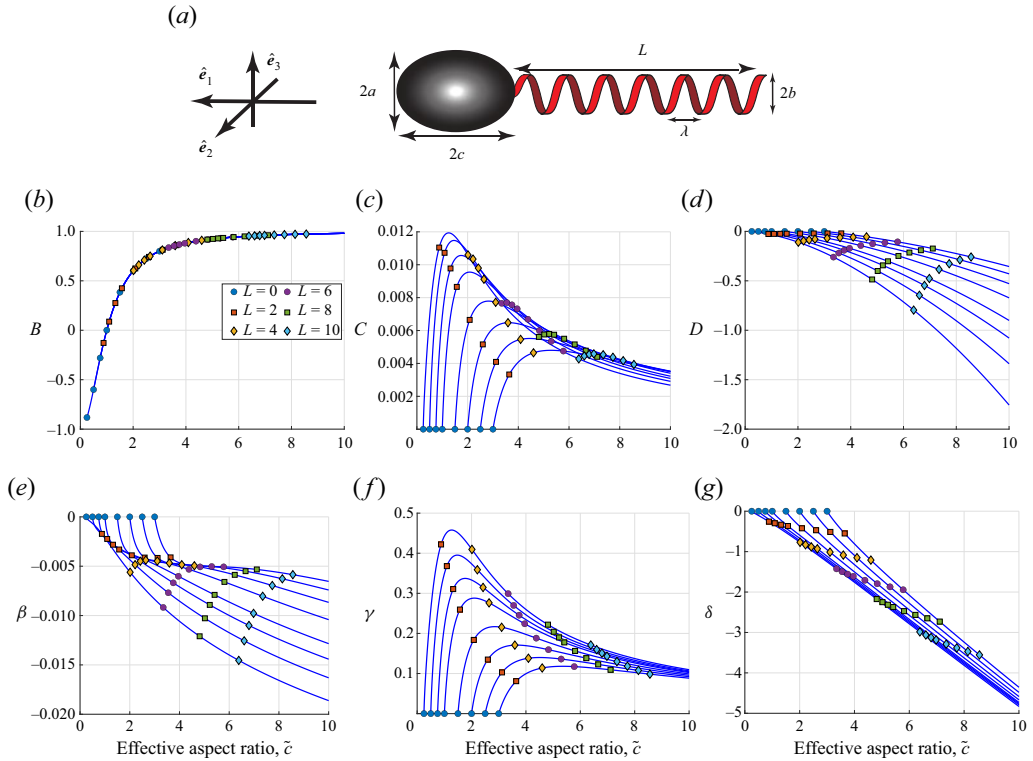
Figure 9. (*a*) Schematic of a model bacterium with a spheroidal cell body and a helical flagellum. The cell body is a rigid spheroid with semi-axes c, a, a, and the flagellum is a simple circular rigid helix with pitch λ, amplitude b and length L. The axis of the helix is $\hat{e}_1$, the director vector of the swimmer. (*b–g*) The values of shape parameters, B, C, D, β, γ, δ for the model bacterium described in (*a*). These parameters are calculated from resistive force theory, using different cell body aspect ratios $c/a \in \{0.25, 0.5, 0.75, 1, 1.5, 2, 2.5, 3\}$ and flagellar lengths L. The horizontal axis represents the effective aspect ratio $\tilde{c}$, obtained from the values of B. The remaining parameters are the same as those used in Ishimoto (2020*a*), and $a = 1$, $\lambda = 2.5$ and $b = 0.25$. The lines represent different values of c. On each line, we use the symbols described in each legend to plot the values corresponding to $L = 0, 2, 4, 6, 8, 10$.

shown schematically in figure 9(*a*). This left-handed simple helix has uniform circular cross-section, with radius b and pitch λ. The flagellum axis and the semi-axis c coincide with $\hat{e}_1$, the axis of helicoidal symmetry.

We calculate the average values of hydrodynamic resistance around the $\hat{e}_1$ axis using resistive force theory and the exact expression for a rigid spheroid. Analytic expressions for these quantities are provided in Appendix B of Ishimoto (2020*a*). We compute the shape parameters from their exact forms, represented by the components in the resistance matrix (Ishimoto 2020*b*). The shape parameters B, C, D, β, γ, δ defined here correspond to $-\beta_2$, β_3, β_1, $-\alpha_2$, α_3, α_1, respectively, in Ishimoto (2020*b*). We plot these shape parameters in figures 9(*b–g*) via the blue lines, with symbols denoting specific values of L.

We vary the aspect ratio of the cell body c/a and the flagellar length L along the $\hat{e}_1$ axis. Additionally, we fix $a = 1$, $\lambda = 2.5$ and $b = 0.25$. We use the cell body aspect ratios $c/a \in \{0.25, 0.5, 0.75, 1, 1.5, 2, 2.5, 3\}$ and flagellar lengths L from 0 to 100. The horizontal axis denotes the effective aspect ratio $\tilde{c}$ obtained from the values of B through

the relationship $\tilde{c} = \sqrt{1+B}/\sqrt{1-B}$. For different values of c, we plot the values with $L = 0, 2, 4, 6, 8, 10$ using specific symbols.

REFERENCES

ARISTOV, M., EICHHORN, R. & BECHINGER, C. 2013 Separation of chiral colloidal particles in a helical flow field. *Soft Matt.* **9** (8), 2525–2530.

BENDER, C.M. & ORSZAG, S.A. 1999 *Advanced Mathematical Methods for Scientists and Engineers I.* Springer.

BRENNER, H. 1964*a* The Stokes resistance of an arbitrary particle – II. *Chem. Engng Sci.* **19** (9), 599–629.

BRENNER, H. 1964*b* The Stokes resistance of an arbitrary particle – III. *Chem. Engng Sci.* **19** (9), 631–651.

BRETHERTON, F.P. 1962 The motion of rigid particles in a shear flow at low Reynolds number. *J. Fluid Mech.* **14** (2), 284–304.

CHEN, P. & ZHANG, Q. 2011 Dynamical solutions for migration of chiral DNA-type objects in shear flows. *Phys. Rev.* E **84** (5), 056309.

DALWADI, M.P. 2014 Flow and nutrient transport problems in rotating bioreactor systems. PhD thesis, University of Oxford.

DALWADI, M.P., CHAPMAN, S.J., OLIVER, J.M. & WATERS, S.L. 2018 The effect of weak inertia in rotating high-aspect-ratio vessel bioreactors. *J. Fluid Mech.* **835**, 674–720.

DALWADI, M.P., MOREAU, C., GAFFNEY, E.A., ISHIMOTO, K. & WALKER, B.J. 2023 Generalised Jeffery's equations for rapidly spinning particles. Part 1. Spheroids. *J. Fluid Mech.* **979**, A1.

EICHHORN, R. 2010 Microfluidic sorting of stereoisomers. *Phys. Rev. Lett.* **105** (3), 034502.

GAFFNEY, E.A., DALWADI, M.P., MOREAU, C., ISHIMOTO, K. & WALKER, B.J. 2022 Canonical orbits for rapidly deforming planar microswimmers in shear flow. *Phys. Rev. Fluids* **7** (2), L022101.

HINCH, E.J. 1991 *Perturbation Methods.* Cambridge University Press.

HYON, Y., MARCOS, POWERS, T.R., STOCKER, R. & FU, H.C. 2012 The wiggling trajectories of bacteria. *J. Fluid Mech.* **705**, 58–76.

ISHIMOTO, K. 2020*a* Helicoidal particles and swimmers in a flow at low Reynolds number. *J. Fluid Mech.* **892**, A11.

ISHIMOTO, K. 2020*b* Jeffery orbits for an object with discrete rotational symmetry. *Phys. Fluids* **32** (8), 081904.

JEFFERY, G.B. 1922 The motion of ellipsoidal particles immersed in a viscous fluid. *Proc. R. Soc.* A **102** (715), 161–179.

JING, G., ZÖTTL, A., CLÉMENT, É. & LINDNER, A. 2020 Chirality-induced bacterial rheotaxis in bulk shear flows. *Sci. Adv.* **6** (28), eabb2012.

KATURI, J., POEHNL, R., SOKOLOV, A., USPAL, W. & SNEZHKO, A. 2022 Arrested-motility states in populations of shape-anisotropic active Janus particles. *Sci. Adv.* **8** (26), eabo3604.

KHATRI, N. & BURADA, P. 2022 Diffusion of chiral active particles in a Poiseuille flow. *Phys. Rev.* E **105** (2), 024604.

KIM, S. & KARRILA, S.J. 1991 *Microhydrodynamics.* Elsevier.

KRAMEL, S., VOTH, G.A., TYMPEL, S. & TOSCHI, F. 2016 Preferential rotation of chiral dipoles in isotropic turbulence. *Phys. Rev. Lett.* **117** (15), 154501.

MA, K., PUJARA, N. & THIFFEAULT, J.L. 2022 Reaching for the surface: spheroidal microswimmers in surface gravity waves. *Phys. Rev. Fluids* **7** (1), 1–13.

MAN, Y. & LAUGA, E. 2013 The wobbling-to-swimming transition of rotated helices. *Phys. Fluids* **25** (7), 071904.

MARCOS, FU, H.C., POWERS, T.R. & STOCKER, R. 2009 Separation of microscale chiral objects by shear flow. *Phys. Rev. Lett.* **102** (15), 158103.

MARCOS, FU, H.C., POWERS, T.R. & STOCKER, R. 2012 Bacterial rheotaxis. *Proc. Natl Acad. Sci. USA* **109** (13), 4780–4785.

MATHIJSSEN, A.J., FIGUEROA-MORALES, N., JUNOT, G., CLÉMENT, É., LINDNER, A. & ZÖTTL, A. 2019 Oscillatory surface rheotaxis of swimming *E. coli* bacteria. *Nat. Commun.* **10** (1), 1–12.

OHMURA, T., NISHIGAMI, Y., TANIGUCHI, A., NONAKA, S., ISHIKAWA, T. & ICHIKAWA, M. 2021 Near-wall rheotaxis of the ciliate Tetrahymena induced by the kinesthetic sensing of cilia. *Sci. Adv.* **7** (43), eabi5878.

RO, S., YI, J. & KIM, Y.W. 2016 Chiral separation by flows: the role of flow symmetry and dimensionality. *Sci. Rep.* **6** (1), 1–10.

RONTEIX, G., JOSSERAND, C., LETY-STEFANKA, A., BAROUD, C.N. & AMSELEM, G. 2022 Rheotaxis of chiral bacteria: from single-cell behavior to a population-level description. arXiv:2204.01492.

SINGH, V., KOCH, D.L. & STROOCK, A.D. 2013 Rigid ring-shaped particles that align in simple shear flow. *J. Fluid Mech.* **722**, 121–158.

THAWANI, A. & TIRUMKUDULU, M.S. 2018 Trajectory of a model bacterium. *J. Fluid Mech.* **835**, 252–270.

WALKER, B., ISHIMOTO, K., MOREAU, C., GAFFNEY, E. & DALWADI, M. 2022*a* Emergent rheotaxis of shape-changing swimmers in Poiseuille flow. *J. Fluid Mech.* **944**, R2.

WALKER, B.J., ISHIMOTO, K., GAFFNEY, E.A., MOREAU, C. & DALWADI, M.P. 2022*b* Effects of rapid yawing on simple swimmer models and planar Jeffery's orbits. *Phys. Rev. Fluids* **7** (2), 023101.

ZHENG, H., YAN, N., FENG, W., LIU, Y., LUO, H. & JING, G. 2023 Swimming of buoyant bacteria in quiescent medium and shear flows. *Langmuir* **39** (12), 4224–4232.

ZÖTTL, A., TESSER, F., MATSUNAGA, D., LAURENT, J., ROURE, O.D. & LINDNER, A. 2023 Asymmetric bistability of chiral particle orientation in viscous shear flows. *Proc. Natl Acad. Sci.* **120** (45), e2310939120.